A Microscale Analysis of Millimeter-wave Induced Vitrified Basalt for Use in Enhanced Geothermal Energy Systems

Rocks and Waves and Glass, O My!

by

Eve Meltzer

B.S., Geological Engineering and Geology
University of Wisconsin, Madison (2020)

Submitted to the Department of Civil and Environmental Engineering in partial fulfillment of the requirements for the degree of Master of Science in Civil and Environmental Engineering at the

Massachusetts Institute of Technology
February 2024

Authored by: Eve R. Meltzer
Department of Civil and Environmental Engineering
January 19, 2024

Certified by: Herbert H. Einstein
Professor of Civil and Environmental Engineering
Thesis supervisor

Accepted by: Heidi Nepf
Donald and Martha Harleman Professor of Civil and Environmental Engineering
Chair, Graduate Program Committee

A Microscale Analysis of Millimeter-wave Induced Vitrified Basalt for Use in Enhanced Geothermal Energy Systems

Rocks and Waves and Glass, O My!

by

Eve R. Meltzer

Submitted to the Department of Civil and Environmental Engineering

on January 19, 2024, in partial fulfillment of the

requirements for the degree of

Master of Science in Civil and Environmental Engineering

Abstract

Extraction of the energy available from geothermal heating in the Earth could provide substantial contributions to energy needs long-term. However, there are major technical limitations with the current geothermal drilling process. A new technology in the field of EGS that uses a millimeter (MM) wave gyrotron, which allows for quicker, more efficient drilling could be a potential solution to these limitations. The MM-wave drilling process, a technique developed by Dr. Paul Woskov of the MIT Plasma Lab, has two significant advantages as compared to traditional drilling: 1. The well hole advance is through melting of the rock, which is faster than mechanical drilling. 2. The molten rock then solidifies, creating a vitrified wall support without the need for extra casings. This drilling and casing process can potentially save money, time, and material. The study presented in this thesis is aimed at understanding the strength and microscale mechanical and chemical properties of the vitrified material to see what is happening to the rock, specifically Basalt, pre- and post-melting by using a series of experimental and analytical tools. These include: Scanning Electron Microscopy (SEM), Electron Dispersive Spectroscopy (EDS), Nano-Indentation, Raman Spectroscopy, and optical imagery.

The results presented in this thesis show the creation of a non-crystalline amorphous solid that has relatively high strength values with slight evidence of micro-cracking. There are significant elemental differences between the basalt matrix, transition zone matrix, and solidified melt in addition to changes in the molecular phases. The partial melting of basalt minerals throughout the transition zone was also recorded. Ultimately, due to micro-cracking and the variability in the transition zone's chemical make-up, there may be significant risks to using this material as a well-bore casing as it is now. However, these results open up the

possibly of future research in the field of environmental sustainability for alternative uses of this new vitrified material.

Thesis Supervisor: Herbert H. Einstein

Title: Professor of Civil and Environmental Engineering

Acknowledgments

I would like to first express my sincere gratitude to my advisor, Professor Herbert H Einstein, for his support, guidance, and insightful feedback throughout my time at MIT. His expertise and dedication has been instrumental throughout my learning process.

To my fellow research group - Randy, Majed, Beatriz, Omar, Rafael, Paris, Ignacio, and Laxman - thank you for exemplifying the qualities of what a graduate student should be. And a special thank you to Beatriz, for early morning office chats and daily encouragement.

To those at MIT who have helped me along the way: Damian Stefaniuk and Professor Admir Masic, thank you for helping me throughout the process and for providing me with an environment that facilitated my research endeavors. Thank you to Dr. Paul Woskov and Quaise for financially supporting me and for introducing me to the world of EGS.

Thank you to those who guided me at UW-Madison: Luke Zoet, Dante Fratta, and Basil Tikoff. You sparked my passion for research in geology and geological engineering and are the reason I am at MIT today.

Special thank you to my family for their encouragement and high expectations that kept me pushing forward.

And lastly, I express my deepest appreciation to my Camberville family. To Church street for endless dinners, Wire episodes, therapy, and for being a second home. To my friends at Das Haus for late night bake sessions and family dinners. To Jurgis and Alfonso for constant encouragement in the form of tea breaks and cards. Without you, I would not have a thesis to turn in.

Contents

List of Figures

List of Tables

Chapter 1

Introduction

1.1 Motivation

With global energy consumption on a continual upward slope, there is a growing need for a clean and renewable energy solution. At present, in the United States, geothermal energy constitutes merely only 2% of the total renewable energy usage. However, both in the U.S. and globally, the utilization of geothermal energy has been steadily increasing. Tapping into the Earth's heat potential holds the promise of significantly reducing CO_2 emissions and making substantial contributions to meet the escalating energy demands worldwide.

Nevertheless, significant limitations currently impede the feasibility of this approach in the United States, creating the necessity of alternative methods. Thanks to researchers at the MIT plasma lab, a novel approach was introduced: the utilization of a Millimeter(MM)-wave gyrotron. This technology potentially allows for the precise excavation of rock by employing MM-wave heating, leading to the melting and vaporization of basement rock at extremely high temperatures. The rapid heating and subsequent cooling of the rock result in the formation of a glass-like substance, making it possible for this melted material to serve as a wellbore casing for geothermal injection and production wells. Thus, in this thesis, I work to understand the mechanical and chemical properties of this new material for possible

use in geothermal wellbore casings as well as other environmental applications.

1.2 Research approach and objectives

The purpose of this research is to develop a strong understanding of material produced from the use of Millimeter waves as a method of drilling into basement rock for the possible use of this material as a geothermal wellbore casing. Achieving this objective involves the use of multiple experimental techniques including Scanning Electron Microscopy (SEM), Energy Dispersive Spectroscopy (EDS), nano-indentation testing, and Raman Spectroscopy. These were specifically chosen to gain a better understanding of the mechanical, thermal, and chemical structure of the rock. Since the samples I have are still in the beginning phase of testing, meaning they are small and fragile, I was not able to perform larger scale mechanical testing and so this micro/nano scale study was conducted. All the samples tested come from the melting of basalt rock. This research focuses on three sections of the sample: the basalt, the transition, and the melt. This is because the sample consists of one larger basalt piece that has been exposed to MM-wave in the center. The transition zone refers to the part of the sample that is between the melt and the host basalt as this zone has clearly been affected by its proximity to the MM waves and has a change of composition and texture, thus it is also important to study and understand.

1.3 Organization of thesis

The remainder of the thesis is organized as follows:

To begin approaching the research objectives detailed in section 1.2, Chapter 2 starts with an understanding of geothermal energy and Enhanced Geothermal Energy Systems (EGS) and how the current technology is used and set up. Following this, a summary of the drilling methods being used in the industry, why they may not be sufficient for EGS

systems, and a small background on the issue of well-bore stability in the oil/gas industry as well as EGS. Next, I discuss the new technology with more detail explaining the hope for how it could improve the industry and how it works.

Chapter 3 introduces my experimental method. I first begin with giving some background on the rock type used in these experiments and talk about the current known literature on heating properties of this rock. I then go through method for sample preparation and discuss the different types of samples I will use throughout the thesis. Finally I go through background on each experimental technique explaining why I chose it, how it's used, and the specific equipment and tests I conduct.

Chapter 4 then details my results for each test and I discuss what these results mean in terms of my objectives. Finally, Chapter 5 wraps up my findings and discusses the future work required to improve and finalize an understanding of this material and its use for geothermal energy

Chapter 2

Background

2.1 Enhanced Geothermal Energy Systems (EGS)

Geothermal energy is a renewable energy source harnessed from the Earth's natural heat, primarily originating from the decay of radioactive isotopes and the planet's original formation. EGS is a subset of renewable energy technologies that harness Earths natural heat for electricity generation via geothermal power plants and with direct use applications for heating. These technologies leverage the Earth's stable and sustainable heat reservoirs to reduce greenhouse gas emissions and reliance on fossil fuels [1].

Shallow geothermal energy systems, which are currently the most common type of geothermal in the United States, typically rely on heat pumps that utilize the relatively stable temperatures of the top few hundred feet of the Earth's crust to heat and cool buildings. These systems are often used for residential and commercial heating and cooling [2]. In contrast, deep geothermal energy systems tap into much hotter temperatures at greater depths, typically through wells drilled thousands of feet deep.

Deep geothermal energy is a renewable energy source that comes from available heat via hydro-thermal resources. These resources are reservoirs of naturally heated water trapped in porous and fractured rock, which are usually found near tectonic plate boundaries [3].

Geothermal power plants harness this hot water to generate steam which in turn creates electricity (Figure 2.1). However, since there are only few of these reservoirs within the Earth, they can be both difficult and expensive to explore. This is why the shift towards Enhanced Geothermal Systems (EGS) could help expand the use of geothermal energy. EGS makes use of geothermal resources sourced from much deeper reservoirs than previously used technology and involves injecting fluid into the Earth, fracturing the deep rock, allowing flow channels to form. This fluid is heated as it flows through the artificially made fractures in the hot rock and is then extracted through production wells. The drilling depths needed for these systems range from about 3,000-5,000 meters with a needed rock temperature range of 180-300°C [4].

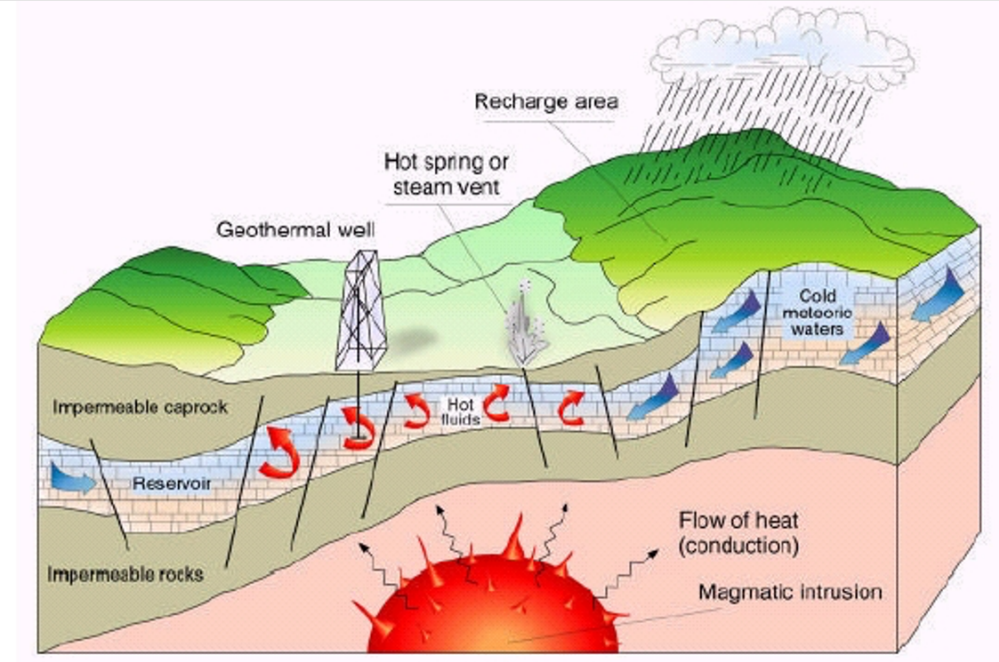

Figure 2.1: Geologic cross section showing hydro-thermal reservoirs and magmatic heat source [5].

2.1.1 Drilling methods

Enhanced Geothermal Systems (EGS) involve creating artificial reservoirs in hot rocks deep in the Earth's crust. The specific choice of location depends on the availability of heat,

the rock's permeability, and the proximity to existing infrastructure. Deep wells, including one or more injection wells and one or more production wells, are drilled into the chosen rock formations. These wells can extend thousands of meters into the Earth. Cold water is then injected into the injection well, which create new or expand current fractures in the rock. This process is known as hydraulic fracturing or "stimulation." The fractures increase the permeability of the rock mass, thus, allowing for improved circulation of water. Once the fractures are created, water is continuously circulated through the EGS reservoir. As it travels through the hot rock, it absorbs heat and rises to the surface through the production well as a high-temperature fluid. The hot water or steam extracted from the production well is used to generate electricity in a geothermal power plant or for other direct-use applications like district heating or industrial processes. After the energy is extracted, the cooled water is typically re-injected into the injection well to maintain pressure and sustain the circulation process. This helps to maximize the efficiency and sustainability of the EGS.

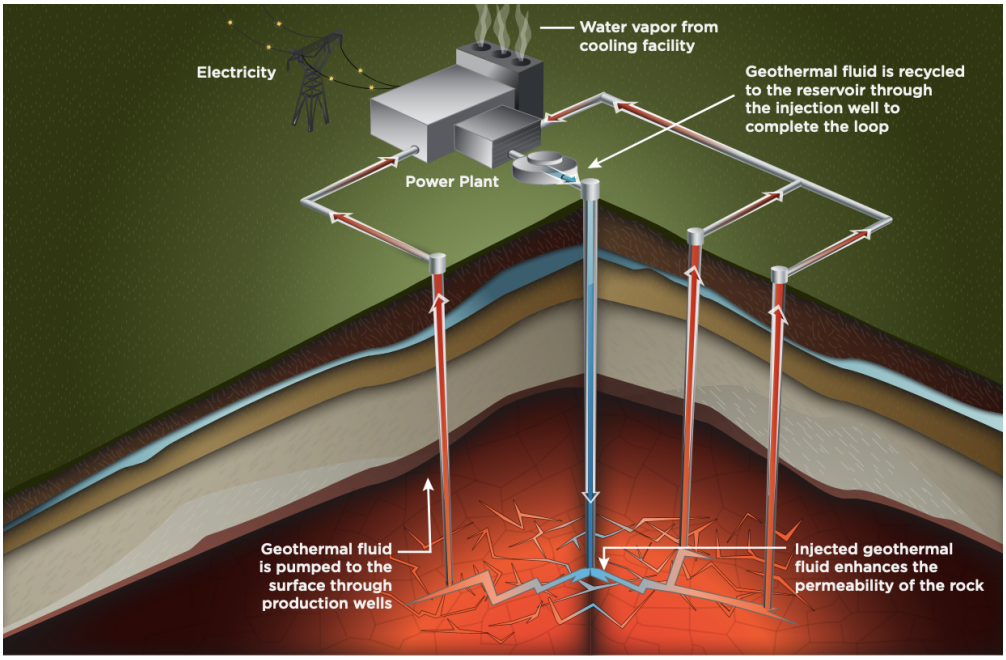

Figure 2.2: Enhanced Geothermal System set-up with fluid injection site and production wells [6].

The current and most common drilling methods for EGS are similar to those for conven-

tional oil and gas wells, such as rotary drilling methods. However, EGS and conventional oil drilling do differ in the formation temperature and penetration rate. The formation temperature, which is the temperature of the rock formations or geological strata where drilling operations take place, in EGS wells is significantly higher and the drill penetration rate is usually lower due to the volcanic or granitic hard and abrasive formations [7]. Both factors make EGS drilling more difficult than conventional oil and gas wells and are the reason for a range of alternative drilling technique's in the field of geothermal energy.

2.1.2 Well-bore stability

Wellbore stability pertains to the ability of an open hole to maintain its required shape, size and structural integrity. It is an important part in minimizing the risk and cost associated with drilling operations. There are both mechanical and physio-chemical related instabilities that can occur in a well. Mechanical instability refers to the stresses, erosion, and pressures while physio-chemical instability refers to the interaction between the drilling fluid and the formation (e.g. possible swelling or dispersion) [8]. One of the main issues with drilling wells is the occurrence of breakouts, which can be controlled by choosing the correct casing design, mud weight (density of drilling fluid), and drilling method [9].

Geologic formations in the Earth at given depths are subjected to vertical compressive stresses, horizontal compressive stresses, and pore pressure. So, when a hole is drilled the rock around must be able to carry the load previously carried by the removed rock [8]. In EGS systems, the wellbores are usually vertical. The vertical principal stress thus act parallel to the wellbore axis while the horizontal principal stresses align perpendicular to the wellbore wall (Figure 2.3). The horizontal stresses can be said to move in the direction of the the minimum horizontal stress (Shmin) and diverge in the direction of maximum horizontal stress (SHmax) which increases and decreases the compressive stress, respectively. This change in stress can lead to borehole breakouts [10]. Due to high probability of failure,

boreholes are usually cased to add support to the surrounding rock walls.

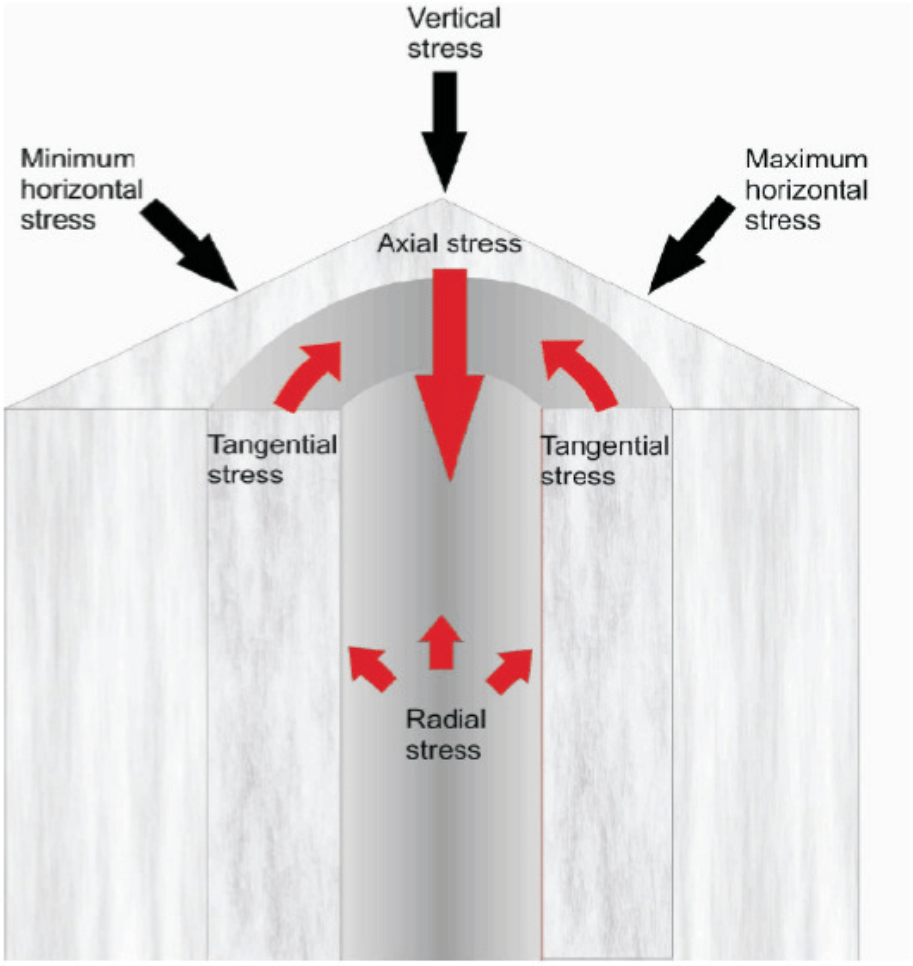

Figure 2.3: Stress distribution around a circular wellbore [10].

The current technologies used for wellbore casings come from the oil and gas industry as well and are an essential component of oil and gas drilling operations. They serve as a protective barrier between the wellbore and surrounding geologic formations. Casing is typically made of steel or other materials with high strength and corrosion resistance, and is installed in sections as the well is drilled deeper [11]. The casing serves to prevent the collapse of the wellbore, control fluid flow, and isolate different zones within the well. Wellbore casings also play a critical role in well completion and production, as they help to maintain the integrity of the well and ensure safe and efficient extraction of resources within the Earth.

Proper design, installation, and maintenance of wellbore casings are essential to the success of drilling operations.

2.2 EGS using millimeter waves

Due to the challenges with ultra-deep drilling, an innovative technology in the field of EGS is emerging that utilizes a millimeter-wave gyrotron for an expedited and more efficient drilling processes. Pioneered by Dr. Paul Woskov at the MIT Plasma Lab, the millimeter-wave drilling technique offers dual advantages over conventional drilling methods. Firstly, it achieves well hole advancement through rock melting, a notably swifter process compared to traditional mechanical drilling. Secondly, the molten rock subsequently solidifies, forming a vitrified wall support without the necessity for additional casings, as outlined by Woskov's research [12]. This vitrified rock casing not only reduces costs and time but also minimizes material usage in drilling operations.

2.2.1 Gyrotron technology

Gyrotrons are a class of high-power linear-beam vacuum tubes and are a powerful millimeter wave source that emit electromagnetic waves at high frequency and intensity. They have recently been used in a new approach to the heating and melting of different materials. The gyrotron is able to rapidly heat a material to up to 3000°C in just a few minutes and has the potential to drill as deep as 20 km to access Earth's temperatures of 500°C.

For the application in EGS drilling, this device uses a metallic waveguide to carry the millimeter wave (MMW) beam to a standoff distance from the crystalline rock. Argon gas is used as the waveguide fill medium due to its ability to stay transparent to MMW's at such deep depths and thus higher pressures [12]. Purge gas is also used to pump out the excess material that has been transformed into smaller particles (Figure 2.4). The energy it takes to melt and vaporize rock can be given by the following formula:

$$H = c_p(T) \cdot \Delta T + H_f + H_v \tag{2.1}$$

where $c_p(T)$ is the heat capacity at temperature T, ΔT is the increase in temperature, Hf is the latent heat of fusion if ΔT includes the melting point, and H_v is the latent heat of vaporization if ΔT includes the vaporization point.

The specific rate of penetration for this device depends on many factors including the beam power, borehole diameter, and required energy as shown below:

$$R_p = \frac{4}{\pi D^2 H} \left(\varepsilon_{mm} P_i - P_L\right) \tag{2.2}$$

where D is the hole diameter, H is the energy given in the previous equation, ε_{mm} is the millimeter-wave emissivity (how well the beam is absorbed by the rock), P_i is the beam power incident on the rock surface, and P_L, is the total power loss from the heated volume.

The gyrotron would only be used on the basement rock and thus conventional rotary drilling is used first to get to the basement rock and then the high powered MMW's are used to drill to the ultra-deep depths. As the MMW beams hit the surface, the rock is melted and then re-solidified into a vitreous material with different properties than that of the host rock. This new vitrified material solidifies around the circumference of the wellbore and could act as a glass casing at deep depths (Figure 2.5).

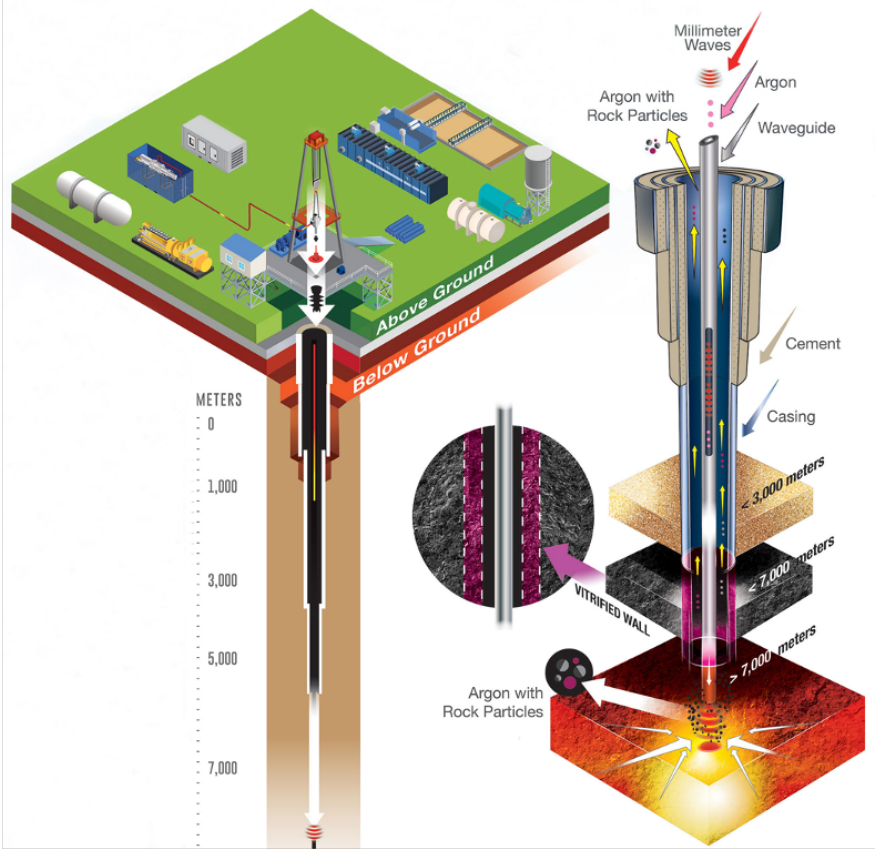

Figure 2.4: Cross section of gyrotron technology for use in EGS drilling [13].

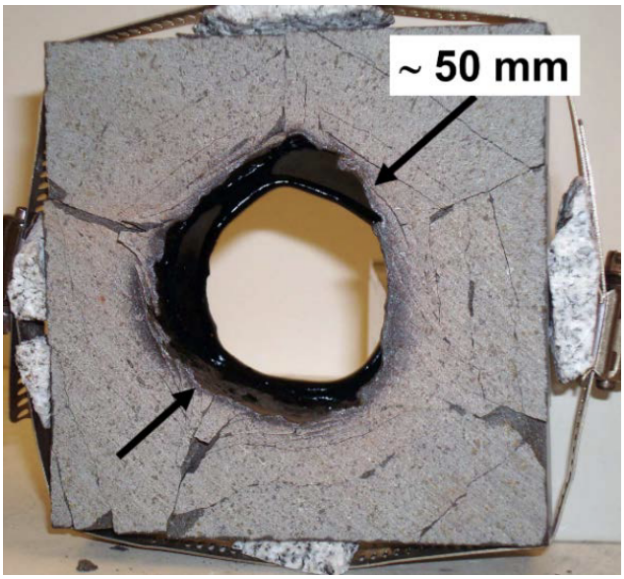

Figure 2.5: Hole in basalt rock that has been created by MMW's with vitrified material on circumference [12].

Chapter 3

Experimental Method

3.1 Rock Materials

3.1.1 Basalt

The rock specimens used in the following experiments consist of basalt rock, which are aphanitic extrusive igneous rocks formed from the rapid cooling of low-viscosity lava. They are usually low in silica ($< 52\%$) and high in minerals such as magnesium and iron. Specifically, these specimens are olivine basalt, also called alkali basalt. This type of basalt rock has a relatively high alkali content, meaning high amounts of sodium and potassium oxide (Na_2O and K_2O). The Total Alkali + Silica (TAS) diagram is shown below, where alkali basalts fall into the top left corner of the basalt box.

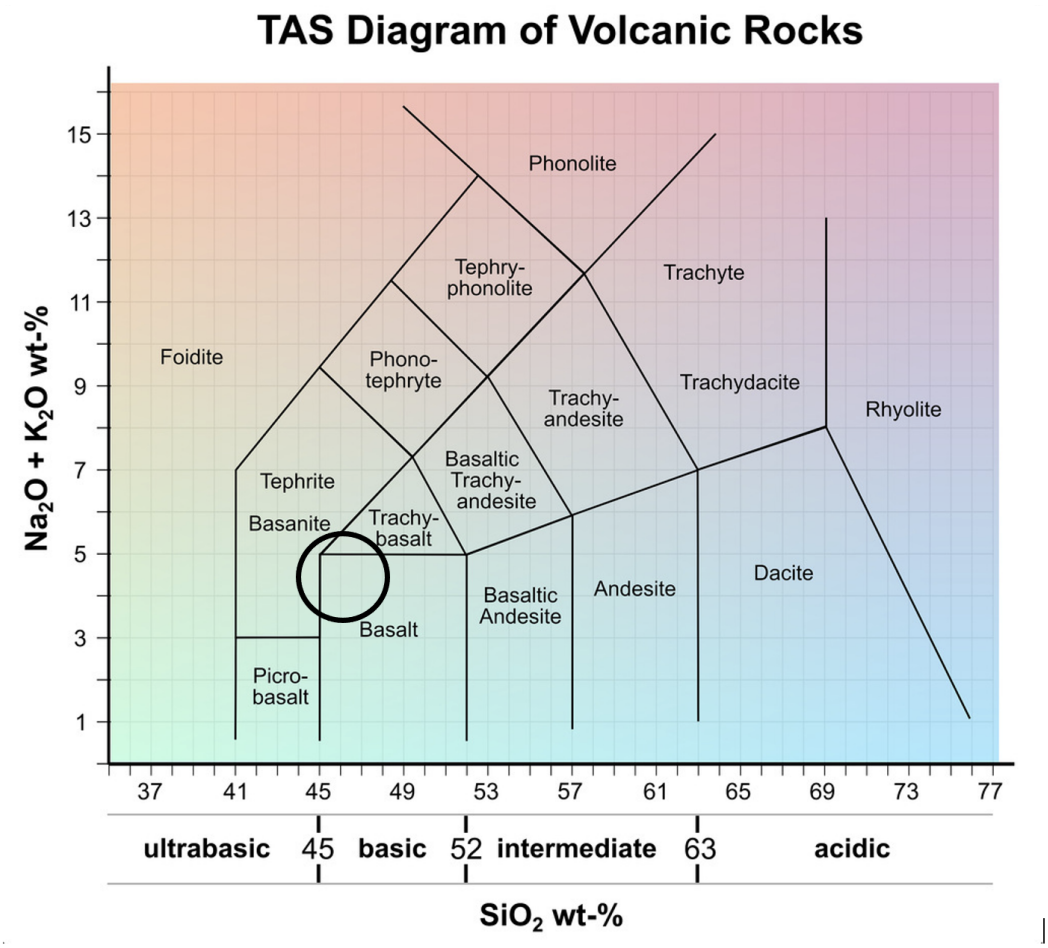

Figure 3.1: Total Alkali and Silica Diagram. The circle indicates location of olivine basalts.

The basalt is encased in a cement mortar to create a rounded specimen and then it is wrapped with a plastic belt to keep the material together while being melted with the gyrotron. After cement and belt encasement the sample is exposed to MM-waves in just the center, with a chosen hole diameter of around four inches. This causes the basalt to melt and cool within just seconds. For the given samples, the melt pools are in the center as shown in Figure 3.2 below.

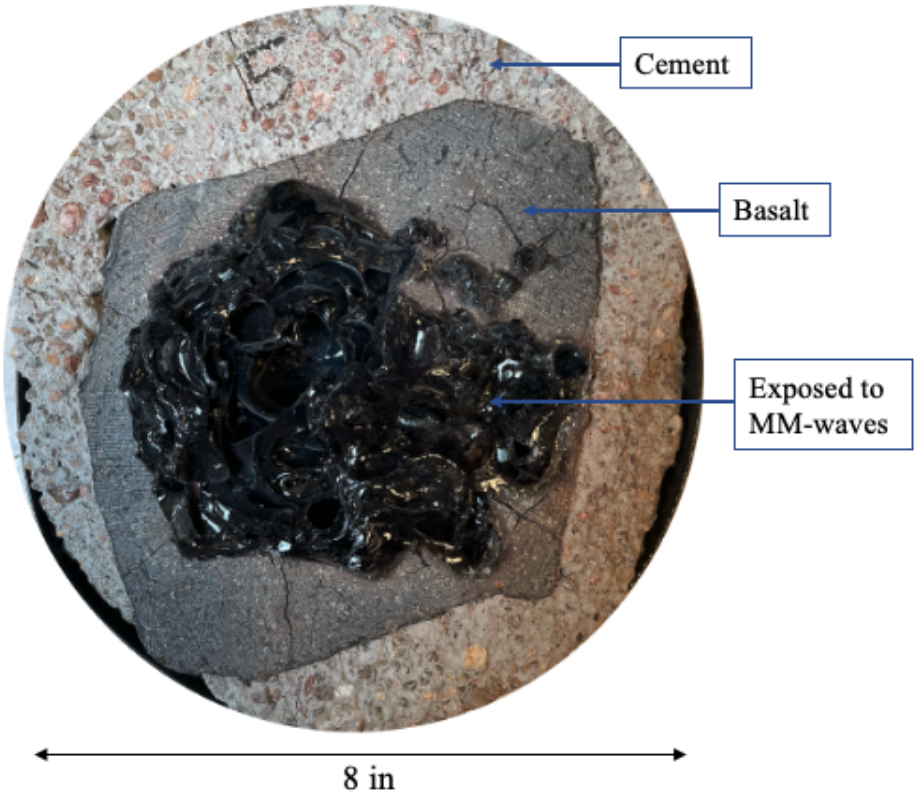

Figure 3.2: Whole rock specimen with melt material in the center

3.1.2 The melting properties of basalt rock

Basalt, primarily composed of silicate minerals with a minor presence of amorphous (glass-like) materials, exhibits diverse physical properties, crystallization temperatures, and strength levels based on its chemical composition. Key chemical constituents include SiO_2, Al_2O_3, Fe_2O_3, FeO, MgO, CaO, Na_2O, K_2O, TiO_2 and more, with feldspar and pyroxene as being the predominant mineral components [14].

The homogeneity of the basalt melt hinges on infusible mineral components and the intricacies of the melting and homogenization processes. Bowen's reaction series, illustrating mineral transformations with decreasing temperature, shows that olivine, pyroxene, amphibole, and biotite sequentially precipitate, with quartz being the final solidifying mineral [15]. Melting and homogenizing basalt containing olivine pose challenges due to olivine's high

melting temperature. Moreover, olivine tends to crystallize early in the cooling process of basaltic glassy melt, potentially causing borehole liner cracking. Consequently, olivine is regarded as an infusible material in basalt melting [14].

Melting process of basalt glass.

No.	Temperature/°C	Reaction
1	0–120	Removal of water
2	350–400	Oxidation on the surfaces of magnetite and ilmenite
3	575	Phase transformation of polycrystalline quartz: α-$SiO_2 \leftrightarrows \beta$-$SiO_2$
4	550–680	Decomposition of carbonates
5	980–1200	Oxidation of magnetite and ilmenite
6	1140–1220	Decomposition of orthoclase, phase transformation, or decomposition of sulfates
7	1200–1300	Melting of plagioclase, diopside, or eutectic compositions, beginning to produce the liquid phase
8	1400–1500	Gradual melting of other mineral components, forming basalt glassy melt
9	>1500	Homogeneous basalt glassy melt

Figure 3.3: Melting process of basalt with the different reactions that occur as the temperature increases[14].

3.1.3 The melt and transition material from MM-wave exposure

The melted then solidified rock has three distinct sections: the basalt, the melt, and the transition material. The basalt refers to the part of the specimen untouched by the MM-waves and thus not melted. The melt refers to the part of the specimen that is fully a vitrified glassy material with a relatively low porosity. The transition refers to the section between the basalt and the melt where the properties and porosity differ significantly. All three sections can be see in Figure 3.4.

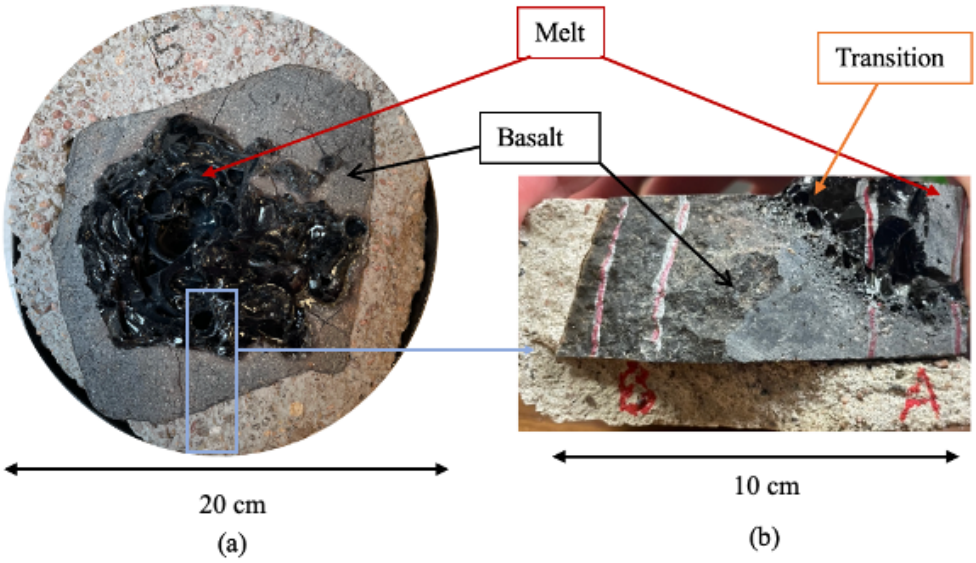

Figure 3.4: (a) Overall image of the sample with melt in the middle. Sample is encased in cement material. (b) Cross section view of the sample cut from the location as the blue box in the figure (and rotated 90 degrees clockwise).

3.2 Sample Preparation

Sample preparation was conducted in three different ways: 1. Samples were cut into smaller pieces straight from the original specimen using a concrete saw and polished on one side. 2. Samples were sent to a thin section company and thin sections were made from the melt material, the basalt, and the transition in between. 3. Samples were cut into smaller pieces, cast in epoxy resin (referred to as "epoxy sample" in the following section), and precision sawed horizontally to create round specimens that are 2.5 cm in diameter, then polished. I will use "overall sample" to specify the entire intact rock that was melted and then specify sample at different scales when referring to the thin section samples etc.

3.2.1 Cut Samples

The cut sections were pieces of the specimen that were taken from the larger sample and made to be approximately 2.5cm in size. They were cut using a concrete saw, which broke the larger sample into pie shaped pieces. The specimen faces were flattened and polished using silicon carbide grinding paper (produced by Buehler) with different grit sizes. The sandpaper with the coarsest grit size was used first, and the finest size was used last. The order of the sandpaper grit size was: N60 → N120 → N220 → N320 → N400 → N600 → N800.

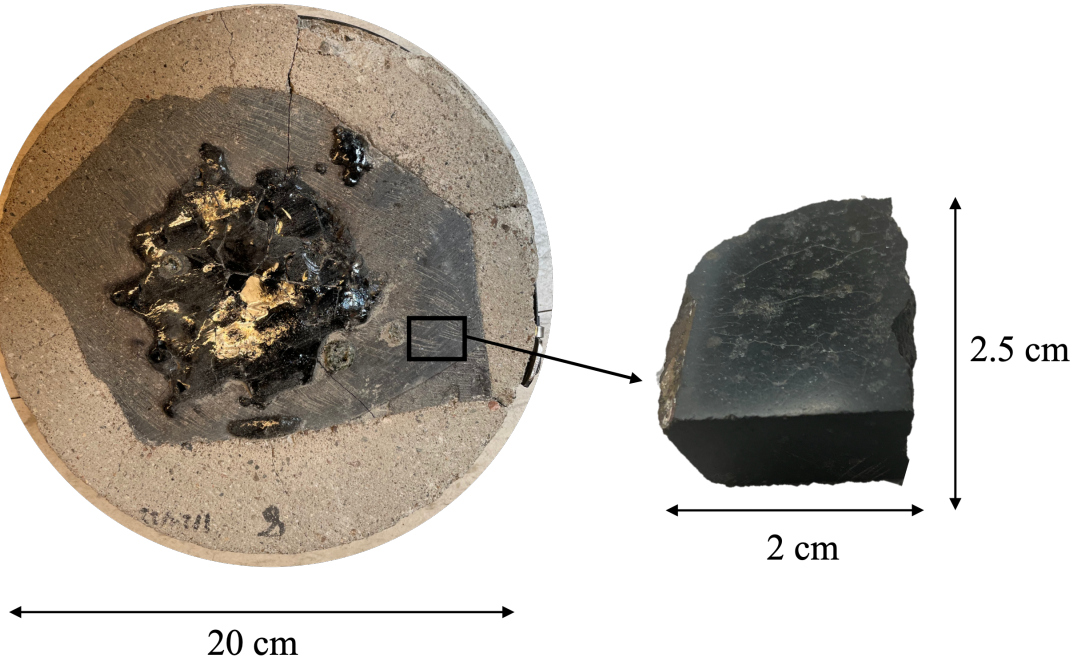

Figure 3.5: The cut sample that used in experimentation is shown on the right and the location it was taken from within the whole sample is shown on the left.

3.2.2 Epoxy Samples

The epoxy samples are made by first placing a small cut piece of the specimen into a clear tube with an approximate diameter of 2.5 cm and a length of 6 cm. Then the epoxy is mixed and poured into the tube until covering the specimen and is first cured in a vacuum

chamber and then rests at room temperature. The rock in the epoxy cylinder is then cut out of the clear tube and the sub-samples, 2.5 cm in diameter and 6 cm in height, are cut from each bulk sample by the use of the diamond saw IsoMet, Buehler (Lake Bluff, USA). This produced cylindrical samples that were 1cm in height. These were then polished with the same procedure used for the cut samples.

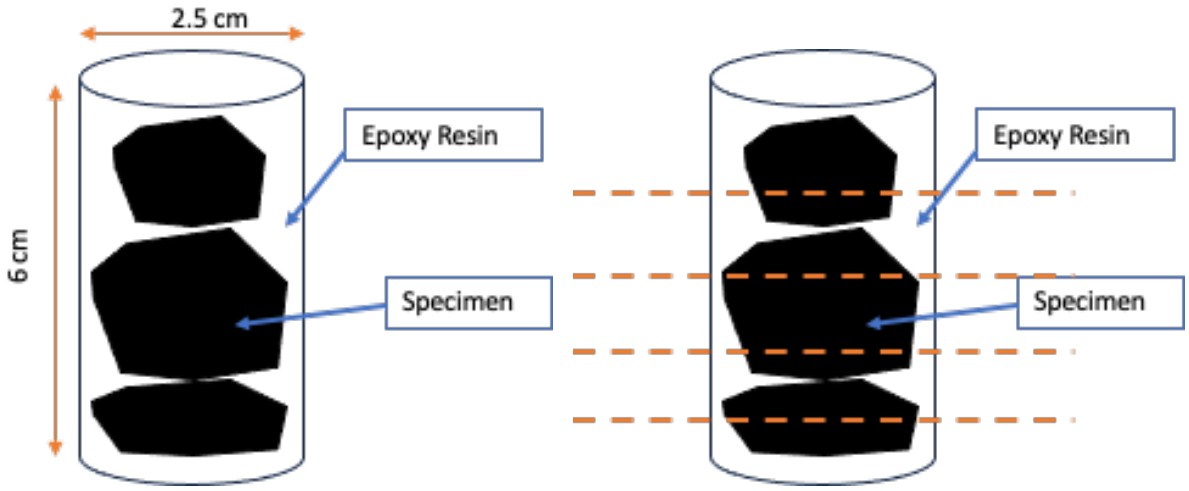

(a) Plastic tube with small specimens stacked on top of one another and epoxy filled to the top (covering samples completely).

(b) Dotted lines are the location of where the diamond saw was used to cut the sample into smaller cylinders after the epoxy cured.

Figure 3.6: Sample preparation for cylindrical epoxy samples.

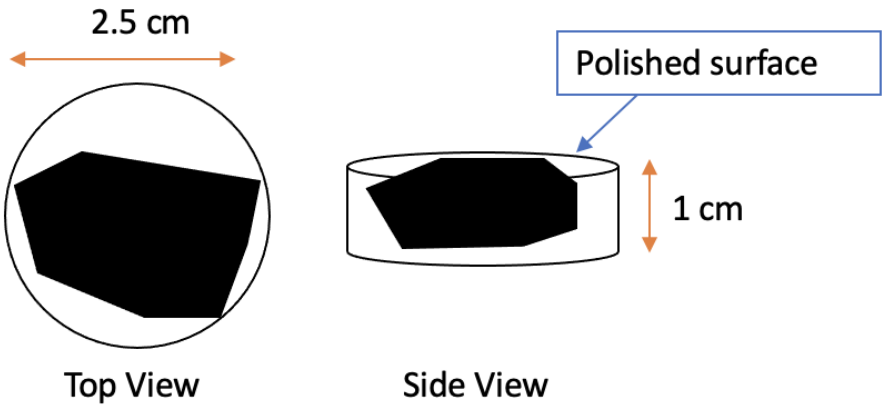

Figure 3.7: Schematic of finished cylindrical epoxy samples

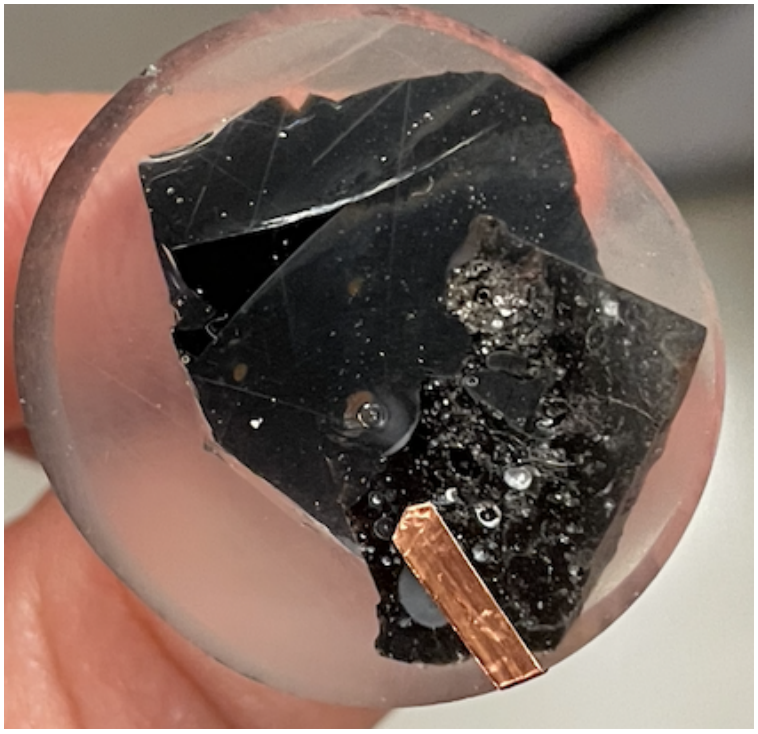

Figure 3.8: Actual sample used for data collection

3.2.3 Thin Section Samples

The original rock sections were cut into smaller pieces using a large concrete saw and then these were labeled with the areas wanted for thin section collection and sent to Spectrum Petrographics (Figure 3.13). The thin sections were cut to 30 micrometers thick and epoxy resin was used in between the glass slide and the specimen (Figure 3.10).

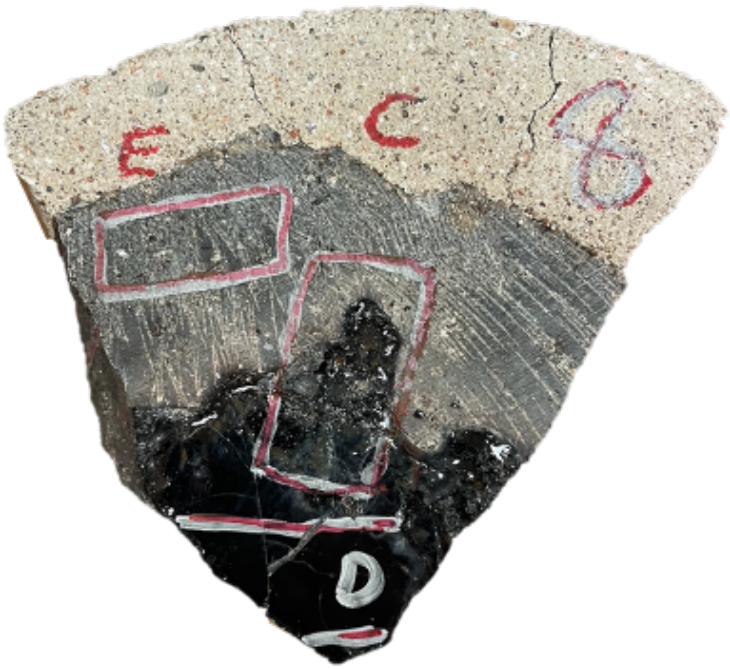

Figure 3.9: Labeled rock section used for thin section making

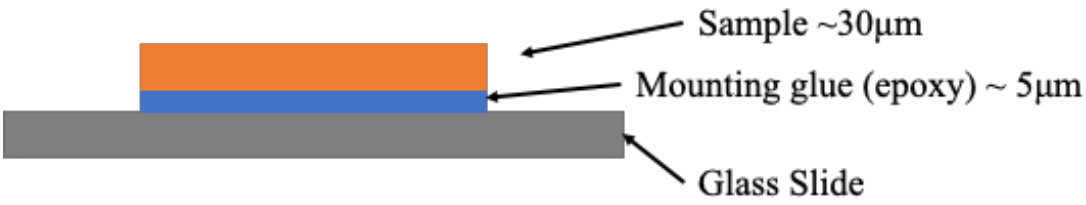

Figure 3.10: Schematic of thin section, showing approximate thickness of each layer.

The schematic in Figure 3.10 was then produced from the rock section to create what is shown in 3.11: the actual thin section sample used in the experiments.

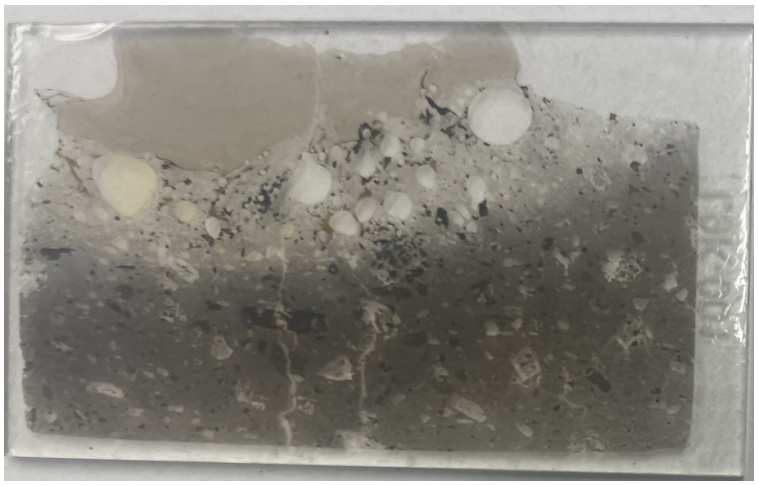

Figure 3.11: Finished thin section used in analysis shown from top view looking down.

3.3 Scanning Electron Microscopy (SEM) and Energy Dispersive X-ray Spectroscopy (EDS)

Scanning electron microscopy (SEM) and energy dispersive X-ray spectroscopy (EDS) are commonly used together in the analysis of rock composition. They are powerful tools in material analysis that can be used to determine the microstructure, composition, and morphology of a specimen. SEM involves the use of a focused electron beam that scans the surface of the rock sample, producing high-resolution images of the sample's topography [16]. EDS, on the other hand, is a technique that allows one to identify the chemical elements present in a sample. It works by detecting the characteristic X-rays that are emitted when the sample is bombarded with electrons.

Scanning Electron Microscopy (SEM) creates high resolution images of the sample. A SEM operates by utilizing a focused beam of accelerated electrons to scan the surface of a specimen. An electron gun generates the electron beam, which is then focused and directed onto the specimen by a series of electromagnetic lenses. As the electron beam interacts with the atoms on the specimen's surface, various signals are generated, including secondary

electrons, backscattered electrons, and X-rays. Detectors capture these signals, and the information is used to create detailed images of the specimen's topography and composition. The scanning motion of the electron beam in a raster pattern across the specimen allows for the construction of high-resolution images [16].

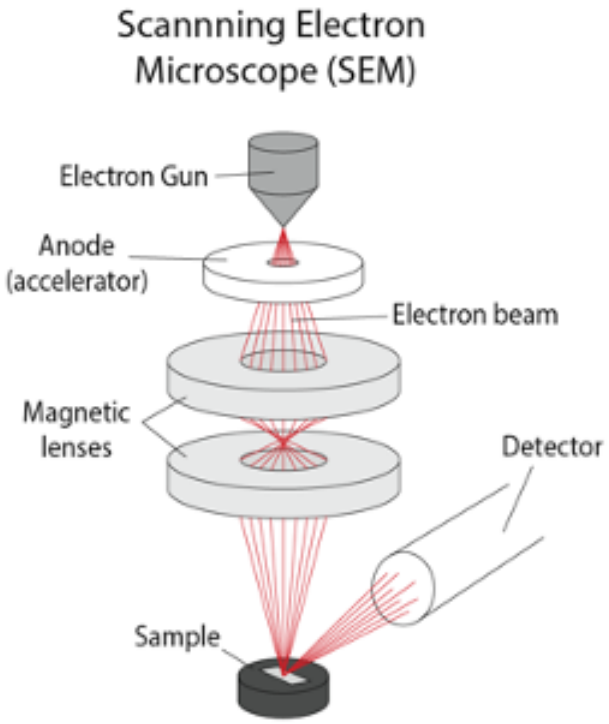

Figure 3.12: Schematic of SEM equipment.

EDS works by detecting the characteristic X-rays that are emitted when the sample is bombarded with electrons. By analyzing the X-rays, elements present within the sample, and their relative concentrations, can be identified. The central component of an EDS system is a solid-state detector, consisting of a semiconductor [17]. As each X-ray photon hits the detector, a very small current is produced by knocking out electrons from the semi-conductor. Each electron ejected from a silicon electron shell consumes about 3.8 electronVolt of energy from the X-ray. By measuring the amount of current produced by each X-ray photon, the original energy of the X-ray can be calculated. An EDS spectrum is essentially a histogram

of the number of X-rays measured at each energy level

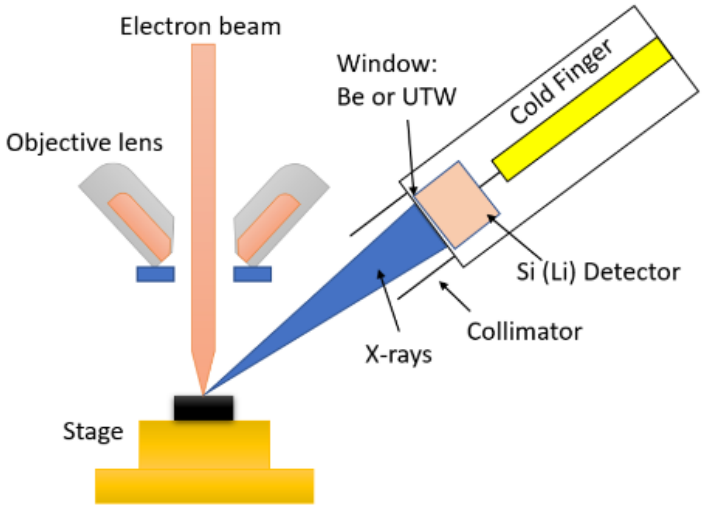

Figure 3.13: Schematic of EDS equipment.

Multi-detector SEM-EDS analyses were conducted on all three zones of the specimen using a Tescan Vega 3 TMU scanning electron microscope, which was equipped with dual Bruker XFlash 5030 X-ray detectors. Traditionally, SEM-EDS element mapping employs a single detector to measure emitted X-rays from the sample, often resulting in a shadowing effect due to topographic obstacles obstructing the X-rays on their way to the detector. In contrast, the use of two diametrically-opposed detectors in multi-detector EDS significantly reduces this shadowing effect, enhancing the reliability of element mapping, especially on rough surfaces.

Mapping data were collected at a 50 mm analytical working distance with an accelerating voltage of 15 keV. Mapping times varied based on map pixel density and elemental abundances and spectra from each pixel were then utilized to calculate elemental ratios.

3.4 Indentation

Nano-indentation is conducted using an instrument called a nanoindenter, which typically consists of a sharp diamond tip attached to a force sensor and a displacement sensor. The tip is brought into contact with the surface of the material to be tested, and a small load is applied, typically in the range of a few millinewtons. The resulting deformation of the material is measured with high accuracy, and the load-displacement data can be used to calculate the mechanical properties of the material such as the hardness and elastic modulus [18]. The indentation depth and contact area can be determined from the load-displacement curve, allowing for the calculation of these properties using the Oliver and Pharr method [19]:

$$H = \frac{P_{max}}{(A_i)} \tag{3.1}$$

$$E_r = \frac{\sqrt{\pi}}{2}\frac{S}{\sqrt{A_i}} \tag{3.2}$$

Where H is the hardness, E_r is the reduced elastic modulus, P_{max} is the maximum load, A_i is the projected area of the indentation, S is the measured stiffness, and v is the Poisson's ratio of the material.

One of the key advantages of nano-indentation is that it allows one to characterize local mechanical properties, rather than averaging over a large volume. By mapping out the local mechanical properties, researchers can gain insights into the small structural features that contribute to the overall mechanical behavior of the material.

Various tip geometries can be employed in indentation tests, and for this study, a Berkovich indenter was used. The Berkovich tip takes the form of a three-sided pyramid, representing a geometric equivalence to a cone with a half-angle of 70.32°.

As with SEM, to perform a nano-indentation experiment, the first step is to prepare a

flat, smooth surface on the material of interest. This typically involves polishing the surface to a high degree of smoothness, using a series of abrasive papers and diamond suspensions.

Indentation tests were conducted using the CSM Instruments standard nanoindentation tester, which was equipped with an environmental control enclosure maintaining conditions at 18 ± 1 °C and 21 ± 2 % relative humidity. The instrument also featured a damping system. Force-controlled tests were performed to a specified maximum penetration depth (hmax = 300 nm). The testing protocol included linear loading and unloading at a constant rate of 12 mN/min, with a dwell time of 5 seconds.

The first nano-indentation test was conducted on an epoxied sample of just melt material with a force of 8 milliNewtons (mN). It consisted of a 25 indent grid. The second test was conducted on a 12mm by 3mm portion of a thin-section that included melt, transition, and host basalt. The location on the thin section was the same location that SEM-EDS and Raman were also tested on. This test was done with a force of 8 mN and included 976 indents with 200 micron spacing between each indent.

3.5 Raman Spectroscopy

Raman spectroscopy is a non-destructive analytical technique used to investigate the molecular composition and structure of materials. The method is based on the Raman effect, which is a scattering phenomenon that occurs when a sample is exposed to a laser beam. In the Raman effect, some of the incident light is scattered inelastically, resulting in a shift in frequency that corresponds to the vibrational modes of the sample's molecular bonds[20]. The resulting Raman spectrum provides information about the molecular composition and structure of the sample, which can be used to identify its chemical composition and analyze its properties.

The basic setup of a Raman spectroscopy system includes a laser source, a spectrometer, and a detector. As seen in Figure 3.14, a laser light source first hits the sample and the light

interacts with the molecules, then the inelastically scattered light is separated into different wavelengths by the dispersive element. Different light of different wavelengths and intensities is analyzed by the detector and converted into the final spectrum.

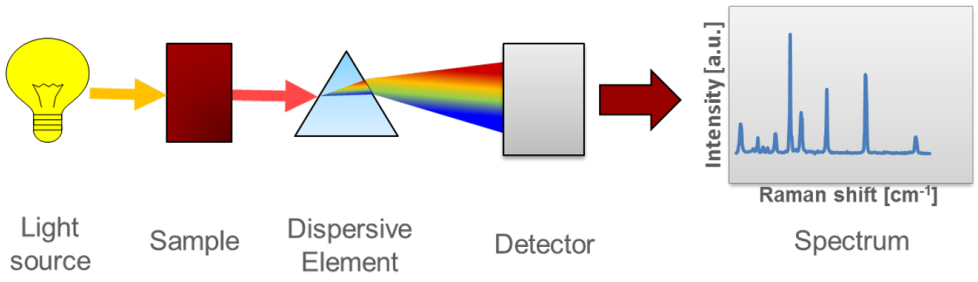

Figure 3.14: Schematic of the measurement principle in a Raman spectrometer

The laser is typically a monochromatic source that emits light at a specific wavelength, such as a helium-neon laser at 632.8 nm or a diode laser at 785 nm. The laser used in these experiments is a green laser with a wavelength of 532 nm and the specific Raman system used is the confocal Raman micro-spectroscopy system (3.15). The laser beam is focused onto the sample using a microscope objective, and the scattered light is collected and directed through a spectrometer to analyze the frequency shifts. The detector records the intensity of the scattered light at each frequency, which is used to generate the Raman spectrum.

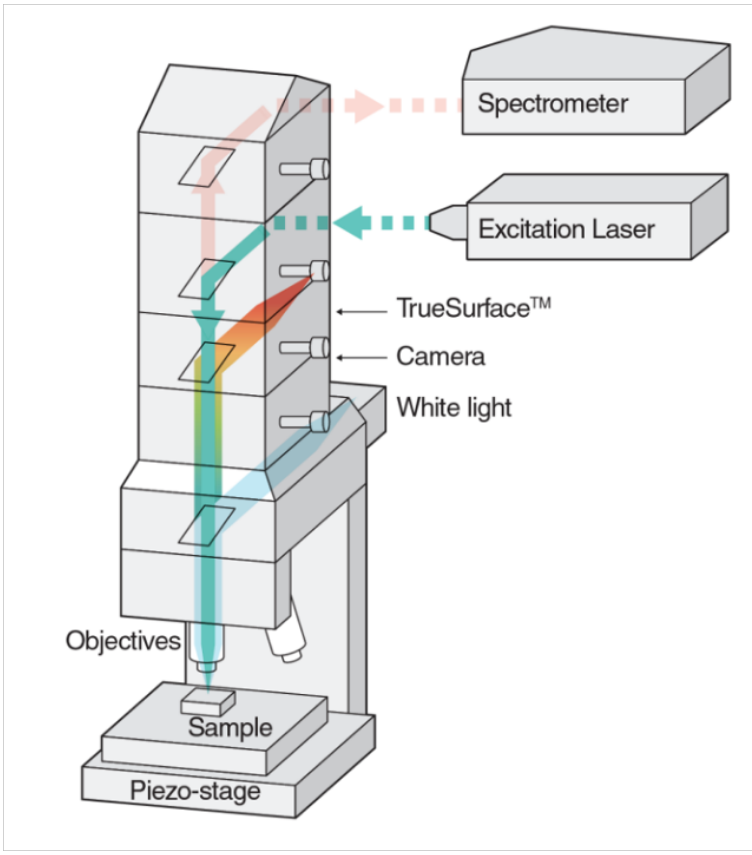

Figure 3.15: Confocal Raman Micro-spectroscopy system

The Raman spectrum produced by a sample can be used to identify its chemical composition and analyze its properties. Different chemical bonds vibrate at different frequencies, so the peaks in the Raman spectrum correspond to specific vibrational modes of the sample's molecular bonds. By comparing the Raman spectrum of an unknown sample to a database of known spectra, the chemical composition and structure of the sample can be determined.

In the analysis of rock material, Raman spectroscopy can be used to identify the specific mineral phases present. It can also be used to determine the degree of crystallinity and the presence of any amorphous or glassy phases[20]. In addition, Raman spectroscopy can be used to study the distribution of trace elements within the mineral lattice, which can provide insights into the formation and evolution of a rock specimen. It is also important to note that since each molecule in a material has a different molecular environment the vibrational energy is affected. This means that the Raman peaks broaden naturally and exhibit peak

profiles similar to those of Gaussian, Lorentzian, or pseudo-Voight peak profiles.

In Raman spectroscopy, a method known as peak profile analysis is used to delve deeper into the characteristics of materials. This technique, as described by Toporski, Dieing, and Hollricher [21], provides three (or four with pseudo-Voight) key parameters—peak intensity (or area), width, and position—that offer valuable insights into the chemical, mechanical, and structural properties of the material being studied. When we talk about peak intensity, we're essentially looking at how strong or weak certain vibrations are within the material. The concentration of vibrational units plays a role in determining this intensity. On the other hand, peak width gives us information about the material's crystallinity and homogeneity. A broader peak suggests a less organized structure, while a narrower one indicates a more ordered and uniform composition. The third parameter, peak position, provides details about the chemical and mechanical environment of the material. Changes in factors like pH, temperature, and stress can be identified through variations in peak position. This parameter acts as a kind of chemical fingerprint, allowing scientists to understand the conditions under which the material exists. Raman peak intensity can also be influenced by the polarization angle. By considering the angle of polarization, researchers can not only refine their understanding of the material's characteristics but also map the crystal orientation of the sample[20]. Peak profile analysis in Raman spectroscopy opens a window into the microscopic world of materials, enabling us to decipher composition, structure, and behavior of materials under different conditions.

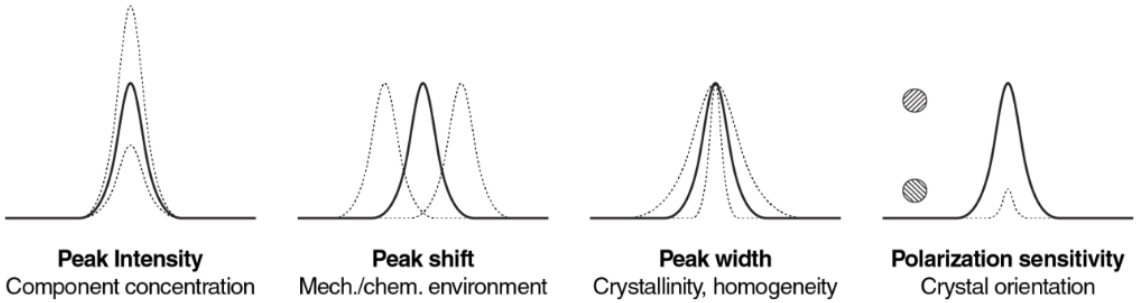

Figure 3.16: The material properties that are related to each peak parameter

The use of Raman spectroscopy for the analysis of rocks is a powerful tool for understanding the mineral composition and structure of these complex materials. Raman spectroscopy can be used to inform a wide range of applications, from the study of geological processes to the development of new materials for construction and engineering.

Chapter 4

Experimental Results

4.1 Scanning Electron Microscopy (SEM) and Energy Dispersive X-ray Spectroscopy (EDS)

Extensive SEM and EDS testing was conducted on all three sample types (cut, thin-section, and epoxy) and in all three regions (basalt, transition, and melt) to gain a better understanding of the samples. This then helped to inform us on how to proceed with further chemical and mechanical testing. Section 4.1.1 analyses the non-melted basalt to get a base understanding of the beginning material. I then discuss the results of the melted (vitrified) material and finally, instead of giving the transition its own section, I discuss all three together. This is because the transition is best understood when analyzing it in context with the whole sample.

4.1.1 Analysis of non-melted basalt

The first sample that was analyzed was a cut specimen from basalt that had not been exposed directly with the MM-waves but was on the outside portion of a whole sample in which the center was vitrified. Figure 4.1 shows an image of the actual cut specimen used and the

location of where it was taken from in the overall specimen.

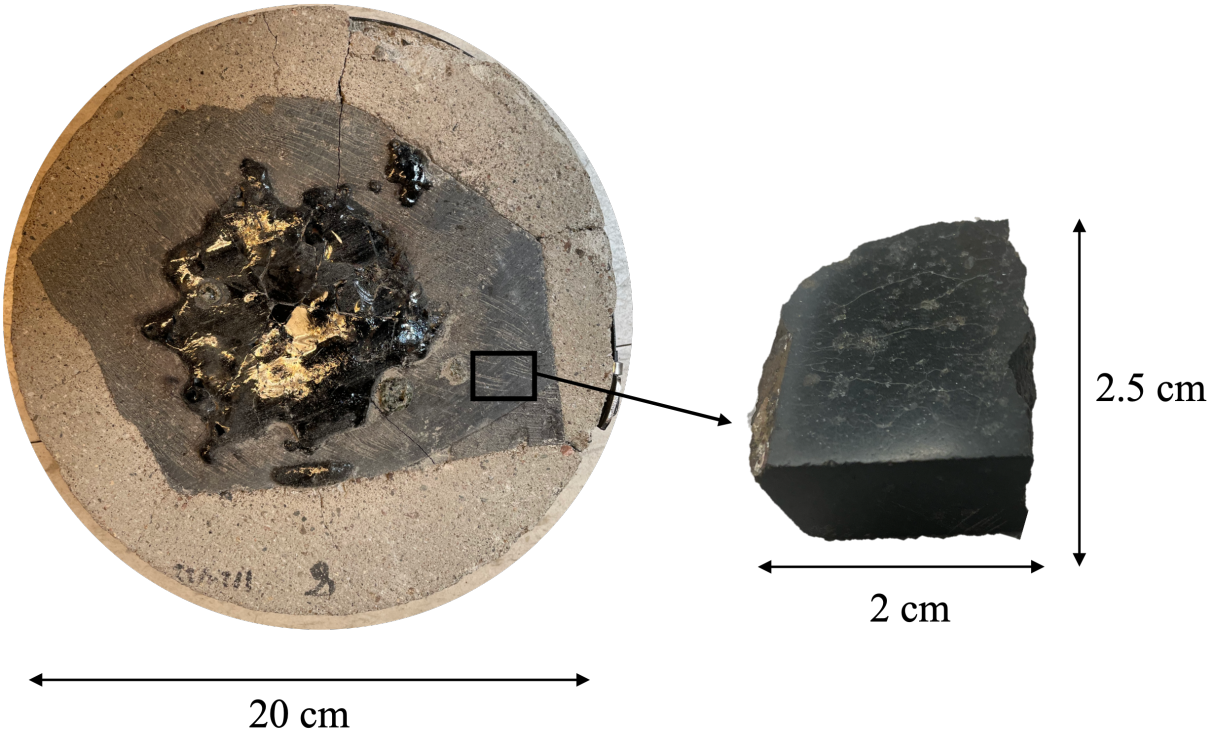

Figure 4.1: Location of basalt cut sample used in first SEM-EDS testing

The first SEM image was taken to get an overall idea of the basalt texture and composition. In Figure 4.2 there is a 3000μm by 3000μm image of the basalt showing the relatively fine matrix with larger phenocrysts. The smaller image, which is 500μm by 500μm, shows a zoomed in image of the phenocryst. It also highlights a radial microcrack that runs throughout the entire sample, but is inter-granular between the two white phenocrysts.

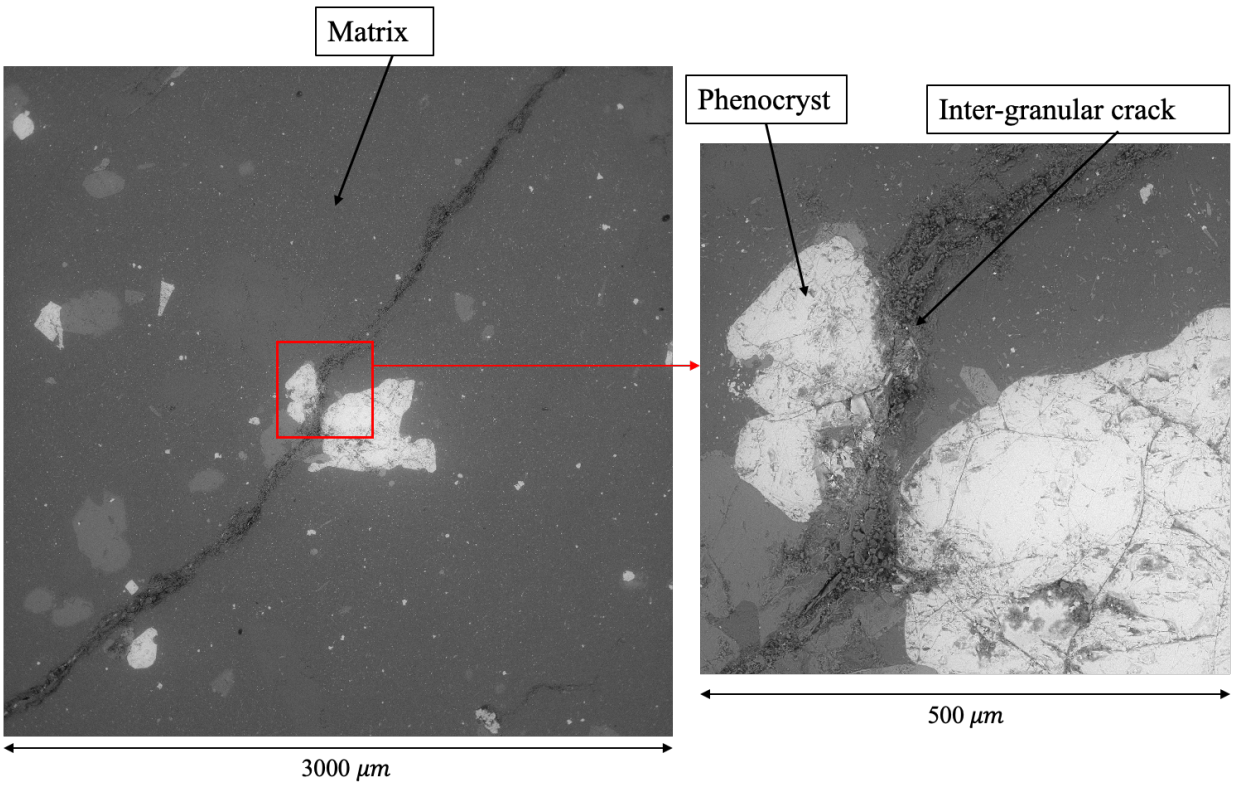

Figure 4.2: SEM images of cut basalt specimen at 3000μm and then zoomed in at 500μm

An EDS map was then conducted on the same 3000μm by 3000μm image of basalt from Figure 4.2, which visualizes the distribution of the constituent elements in the specimen by two-dimensionally displaying the characteristic X-ray intensities or the concentrations of the elements [22]. Figure 4.3 shows the results from this test where each image indicates the spatial distribution of elements throughout the sample. The lighter the color, the more that element is present in that location. For example, looking at the Iron (Fe) map, the larger white phenocryst is illuminated along with smaller minerals throughout the matrix and thus these areas have high iron content as compared to the rest of the specimen. Almost all of the basalt contains oxygen and silica while the matrix is high in carbon, potassium, and sodium. This is fitting with the known components of igneous mafic rocks.

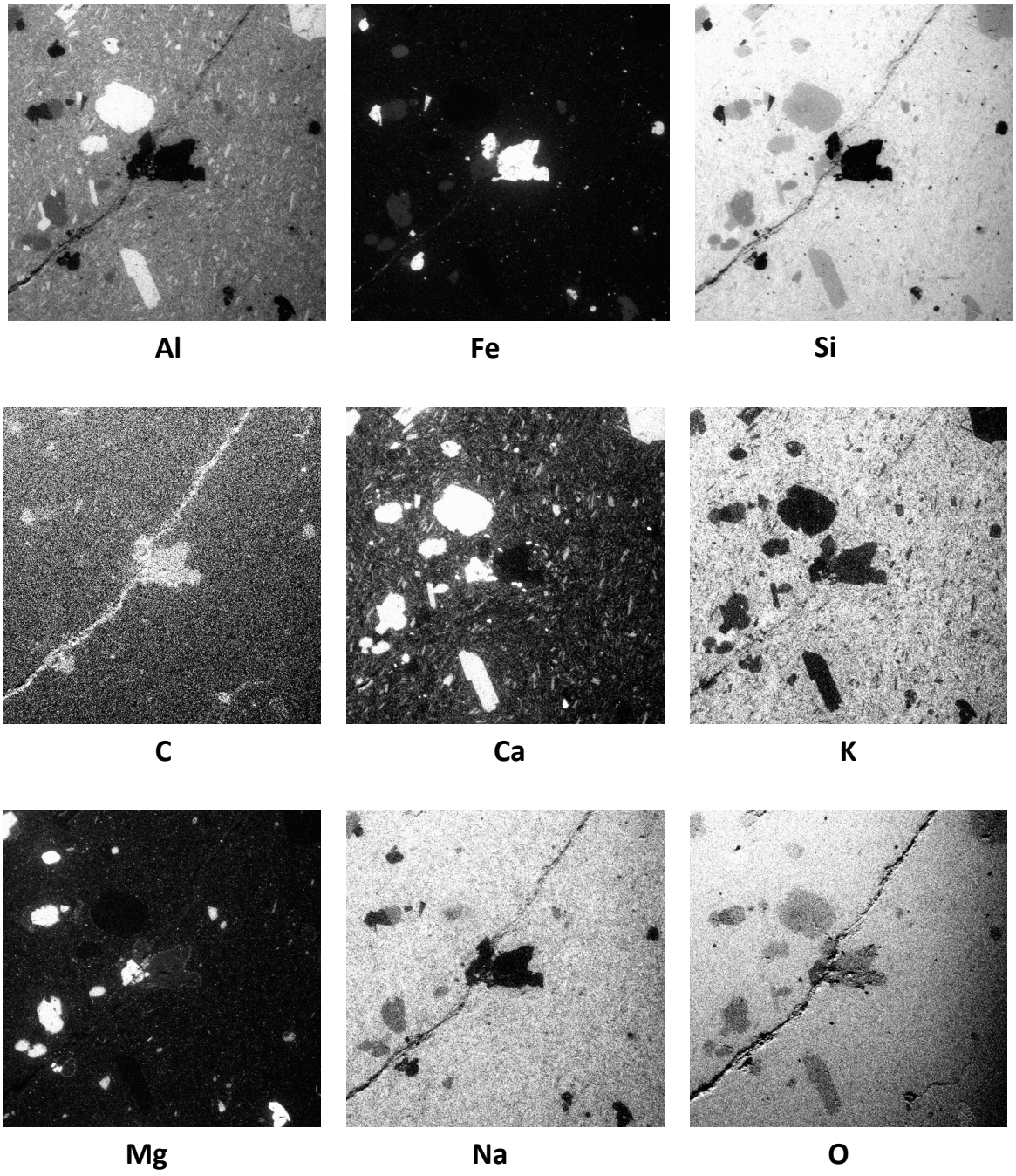

Figure 4.3: Distribution of constituent elements on basalt sample (SEM image of same sample shown in Figure 4.2)

Next, on this same image as above, specific points were chosen to get a more in-depth chemical analysis of both the larger grains and the matrix. Each point gives the atomic

concentrations of elements in that location, which are then plotted for comparison (Figure 4.4). In EDS testing, all points include about 50% atomic concentration of oxygen; This value was removed from the final results and the remaining atomic concentrations were re-normalized 100%. This was done to get a better representation of the important elements within the sample. These results show again the presence of iron bearing minerals (point 2), magnesium bearing minerals (points 3,4,6) and areas with an increase in calcium and aluminum. Two Points 7 and 8 were chosen in the matrix and these include glass phases as well as varying amounts of all the elements. By glass, I am referring to the amorphous solid produced from the rapid melting and cooling of rock material, meaning they no longer exhibit an ordered crystalline structure. The glass in this basalt is composed primarily of SiO_2.

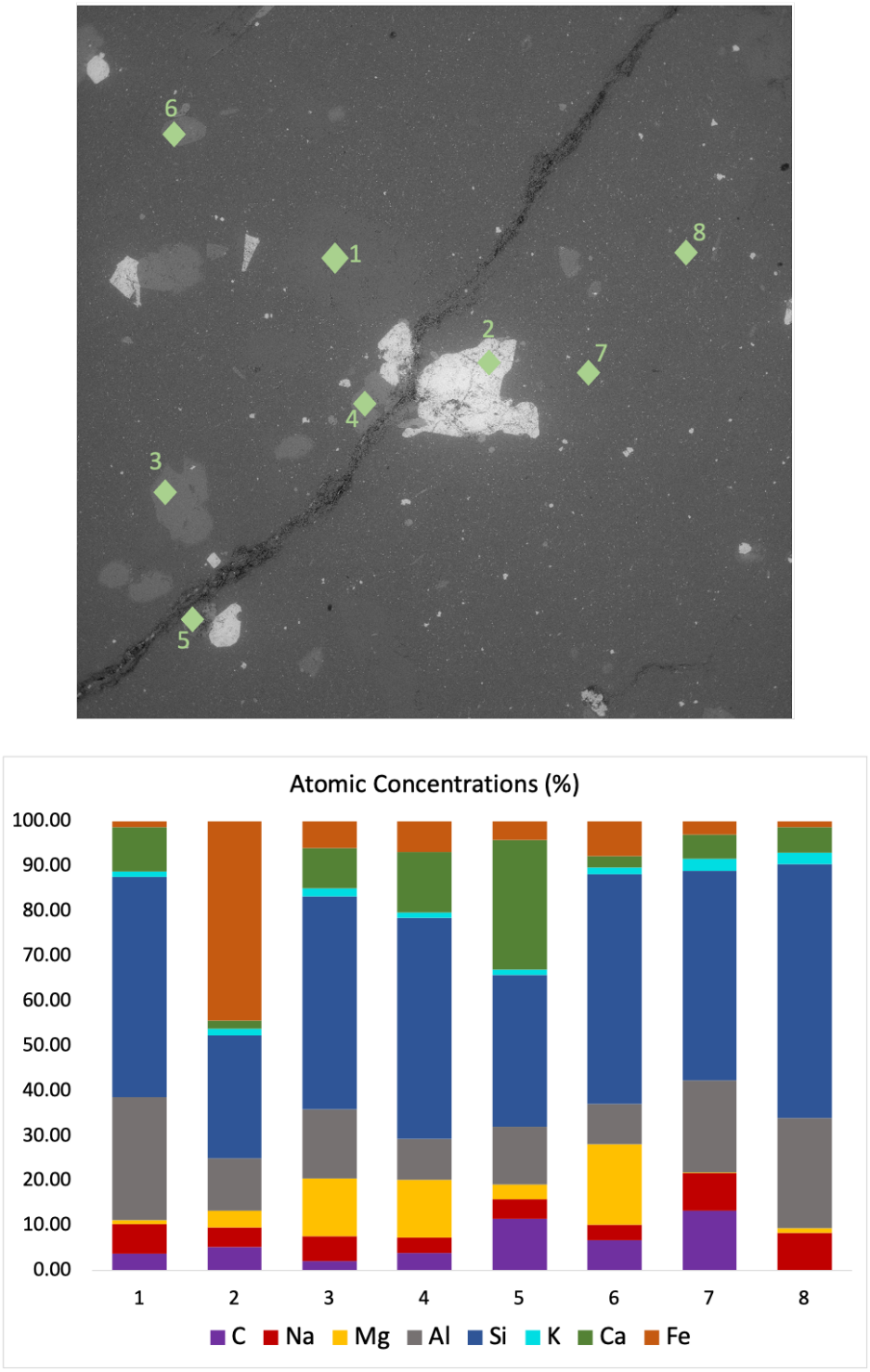

Figure 4.4: Point mapping in EDS with the corresponding elemental atomic concentrations.

Using the spatial elemental distributions, a color map was produced highlighting the important elements within the sample. This gives a better visual understanding of the ele-

ments present within the matrix and larger minerals with clear distinction of the magnesium bearing and iron bearing minerals within the aluminum matrix. This was also used for mineral identification, which was done using all three experimental methods, along with optical imaging.

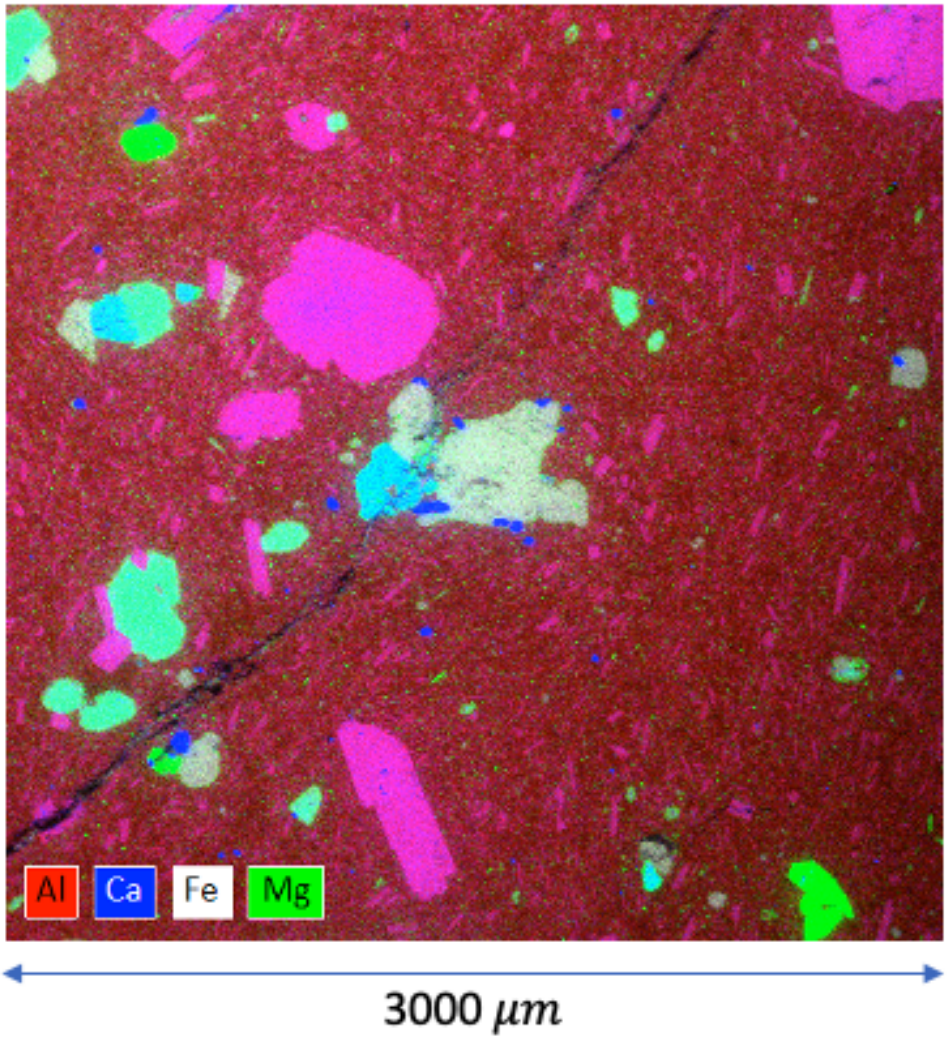

Figure 4.5: EDS color map indicating important elemental distributions. Multiple elements within one location create a mixture of different assigned elemental color e.g. pink minerals are a mix of aluminum (red) and iron (white).

These SEM-EDS results confirm the pre-known knowledge of basalt compositions, as discussed in Chapter 3.1.2, with the presence of plagioclase feldspar, olivine, and pyroxene minerals in a silica and aluminum matrix. With this information, and the knowledge of

where the iron and magnesium bearing minerals are within the matrix, we can pick specific locations for Raman and indentation testing to also gain an understanding of the mineral phases and what is changing post melting.

4.1.2 Analysis of vitrified material

The SEM-EDS analysis of the melted region included both epoxy and thin section sample types. Figure 4.6 is an SEM image of a cylindrical epoxy sample of just the melted region at both 500μm and then zoomed in at 50μm. As shown, the melt is an extremely homogeneous, amorphous material due to the rapid cooling and solidification of the melted basalt. It contains just small circular structures, most likely formed from gas bubbles within the melted region.

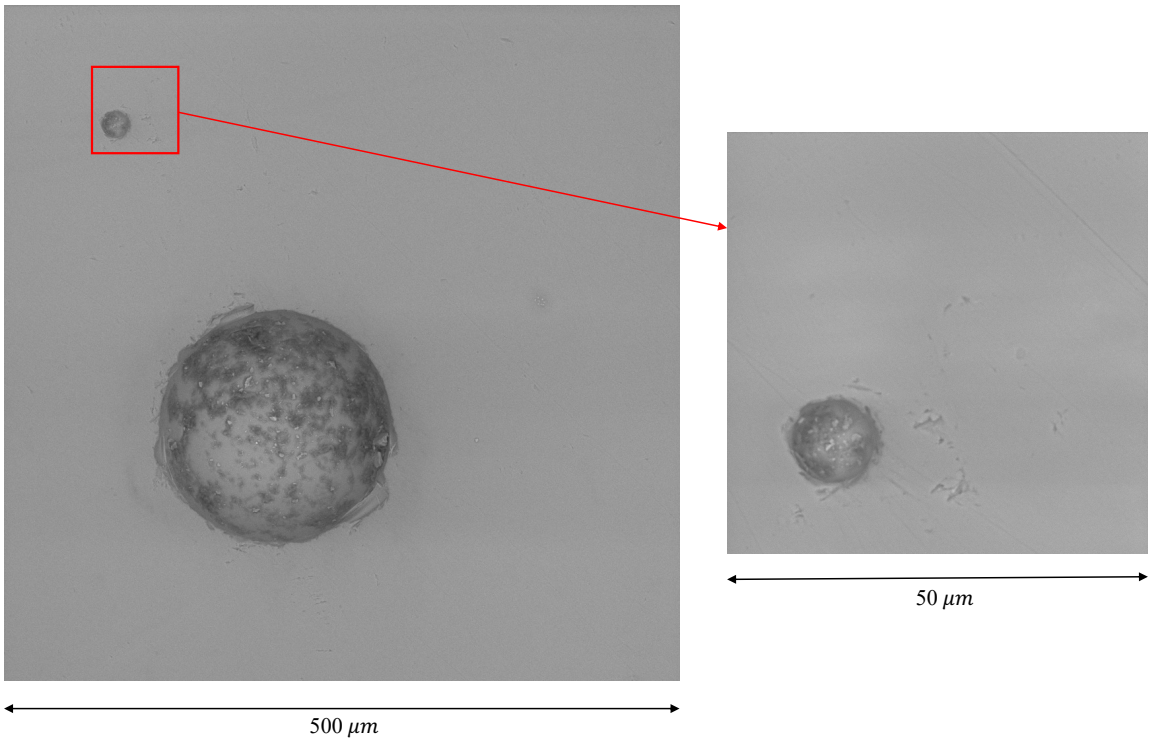

Figure 4.6: SEM image of the melt region in an epoxy specimen

The SEM results from the melted region also show micro-cracking structures (Figure 4.7). Both the images below are 3000μm by 3000μm in size and the arrows indicate the location of cracking. These could either be a result of the quick thermal decrease during cooling or after solidification as this region is then relatively brittle.

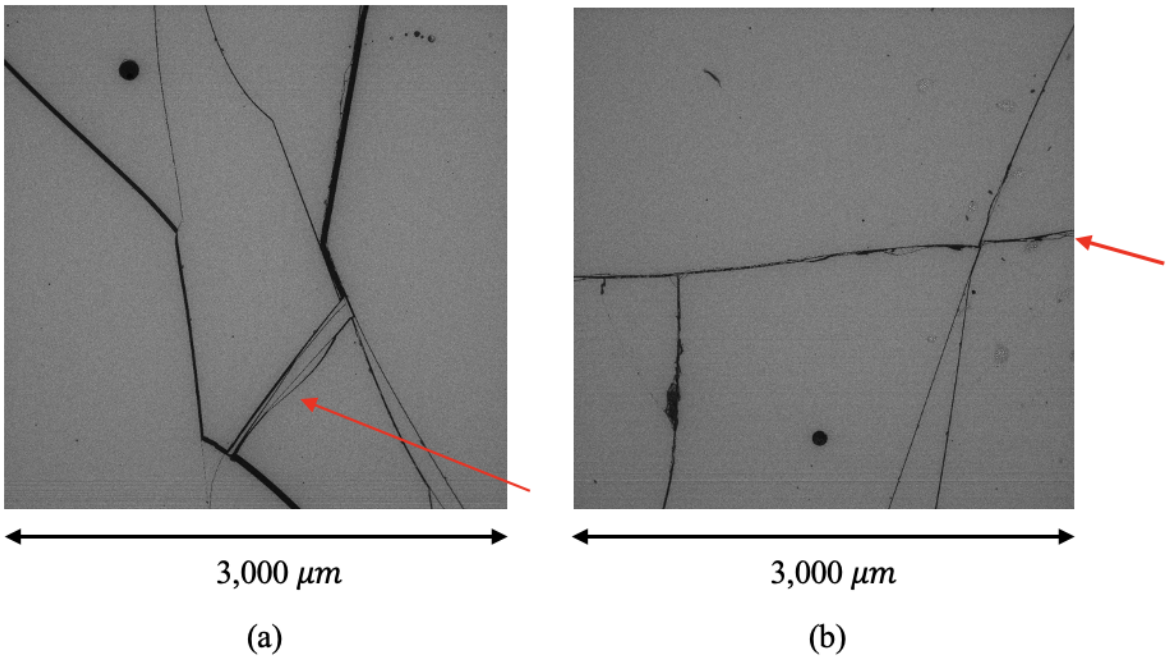

Figure 4.7: SEM images of a thin section taken from the melt region of the specimen showing micro-cracking (indicated with red arrows).

Next, SEM-EDS was conducted on a thin section sample of just the melted region where there was micro-cracking throughout. Four points were taken and averaged together as they all had the same elemental composition. This result was then plotted on a pie chart as shown in in Figure 4.8. These results again are atomic concentrations with oxygen removed and recalculated to 100% (oxygen was at 52%). The melt is made of primarily silica and carbon with large amounts of aluminum and sodium. The carbon is most likely due to dissolved CO_2 in the basalt melt.

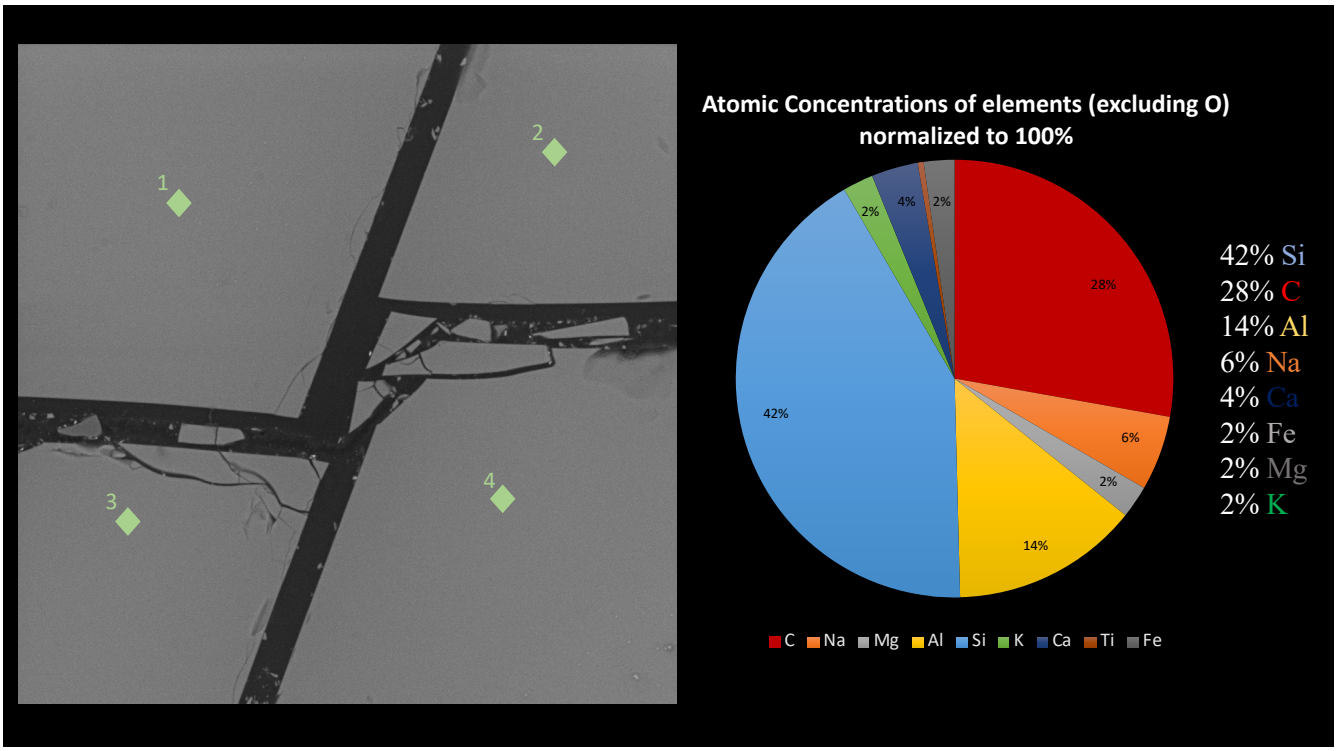

Figure 4.8: Point analysis for atomic concentrations of elements in the melt. Each green triangle corresponds to a location where EDS was conducted. The pie chart shows the average distribution of the elements found in this test. Melt is composed primarily of Si, C, and Al.

4.1.3 Analysis of all three sections

A larger image was then taken of a thin section sample that included all three zones, showing the transition between each. This sample is approximately 12mm long and 3mm wide. From this image, EDS was used to produce a colored elemental distribution map (Figure 4.9). The map shows the full transition from basalt to the vitrified region with the presence of Mg, Ca, Fe, and Si highlighted (the purple is indicating the presence of aluminum). Within this transition you can see an increase in pore size and distribution and then a quick shift to low pore density in the melted region. The EDS map also shows the presence of the iron and magnesium bearing minerals in basalt, as seen from the previous EDS test, and how these elements then redistribute throughout the sample in the transition zone and melted region. Notice the magnesium bearing mineral in the basalt appears partially melted within

the transition zone. This is most likely due to partial melting in the zone right outside the area being exposed to MM-waves, meaning that the heat from the MM waves have affected the area right outside the beam and not just where it is hitting the sample. These phase changes cause significant impact on the its strength and durability of the transition zone.

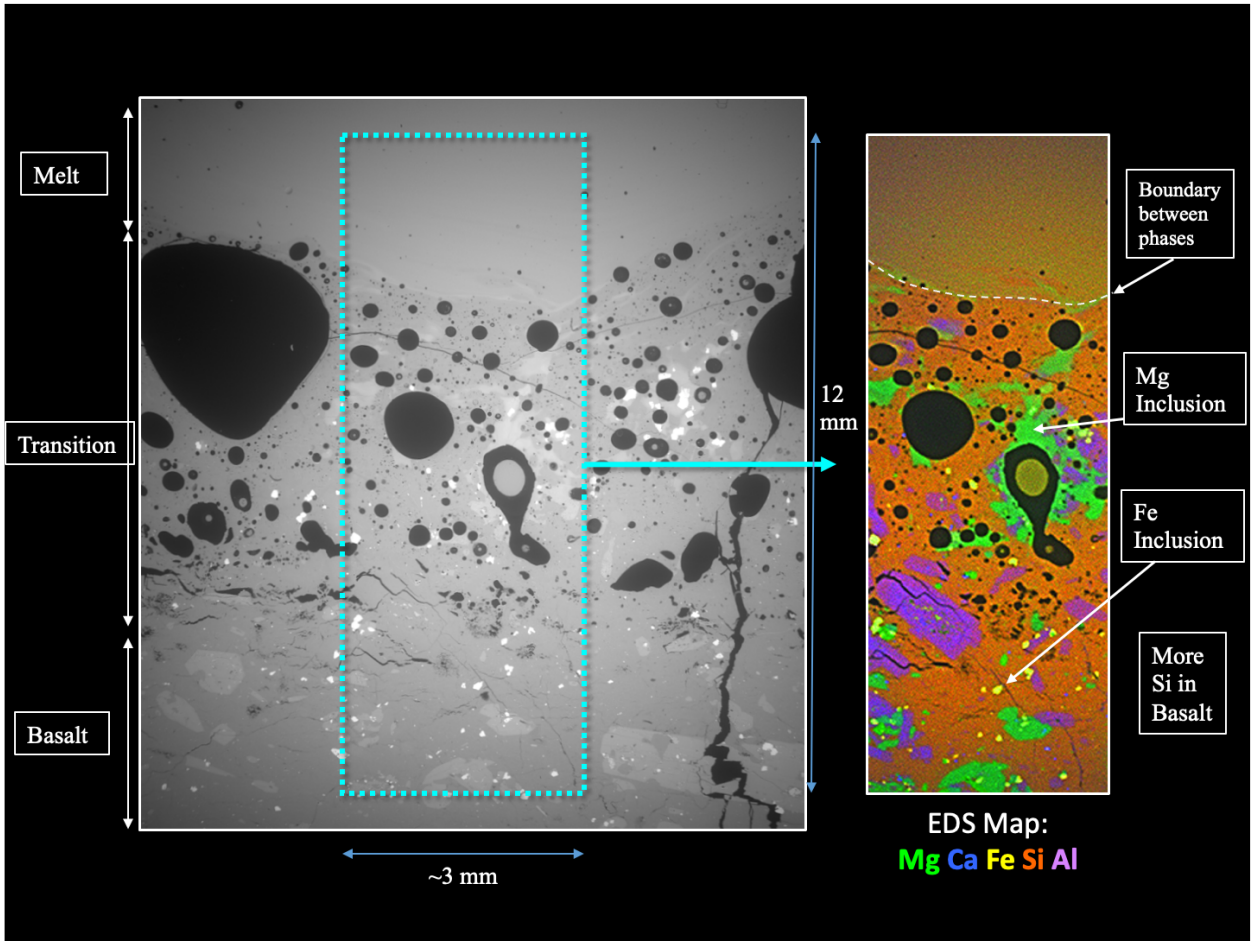

Figure 4.9: The SEM image used in EDS analysis with a color map indicating concentrations of certain elements

On the same thin section sample, specific points were chosen along the specimen in the matrix of the basalt and then throughout the matrix of the transition and into the glass region to understand elemental changes. These values are then plotted, showing the change in atomic concentrations of elements in the matrix of the basalt through the transition into the melted region (i.e. no inclusions). Each point on the graph corresponds to a point on the sample directly above (Figure 4.10). Sodium and silicon are decreasing as one moves

from the basalt to the glass region with more variation in the transition zone. Magnesium and iron increase while calcium and aluminum seem to have only slight changes. This is most likely due to 1. the mixing of elements that make up the minerals in basalt (but not the matrix) and 2. the possible oxidation of a few elements due to such high temperature exposures.

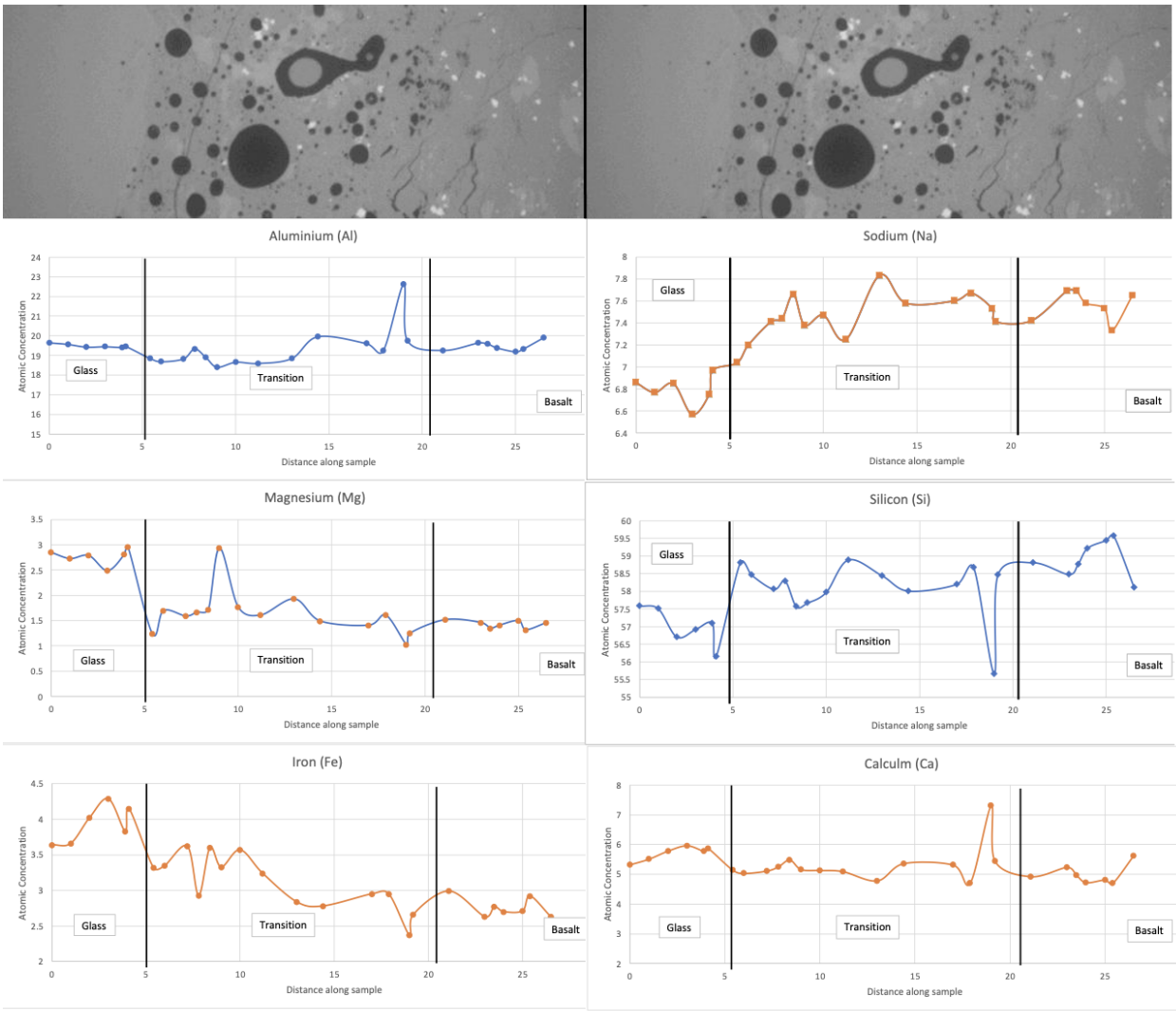

Figure 4.10: SEM-EDS results showing the atomic concentrations of elements along an SEM image of a thin section. Black lines indicate a change from glass to transition to basalt material.

4.2 Indentation

Two nano-indentation tests were conducted, the first was on an epoxy sample that only included the melted region. The second test was much larger and conducted on a thin section sample that included all three zones (basalt, transition, and melt). This exact thin section sample was the same as used in EDS and Raman testing for further comparisons.

4.2.1 Nano-indentation of melted region

The first test, conducted on only the melted region of an epoxy sample, included 25 indents and of those, 23 were usable. This is because two of the indents hit small pores within the sample and so they were not able to get an accurate value. The sample used, positioned on a metal stage, is shown in Figure 4.11 below.

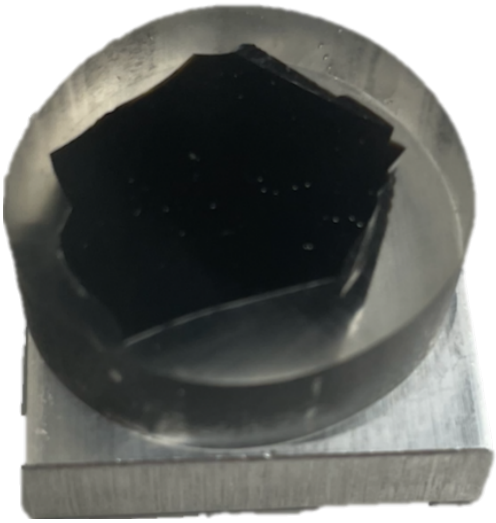

Figure 4.11: Actual epoxy sample used in the first nano-indentation test.

The indents were spaced evenly in a 5 by 5 grid pattern. 4.12 is an optical image (71μm by 51μm in size) showing the actual indents, which are the bright green triangles.

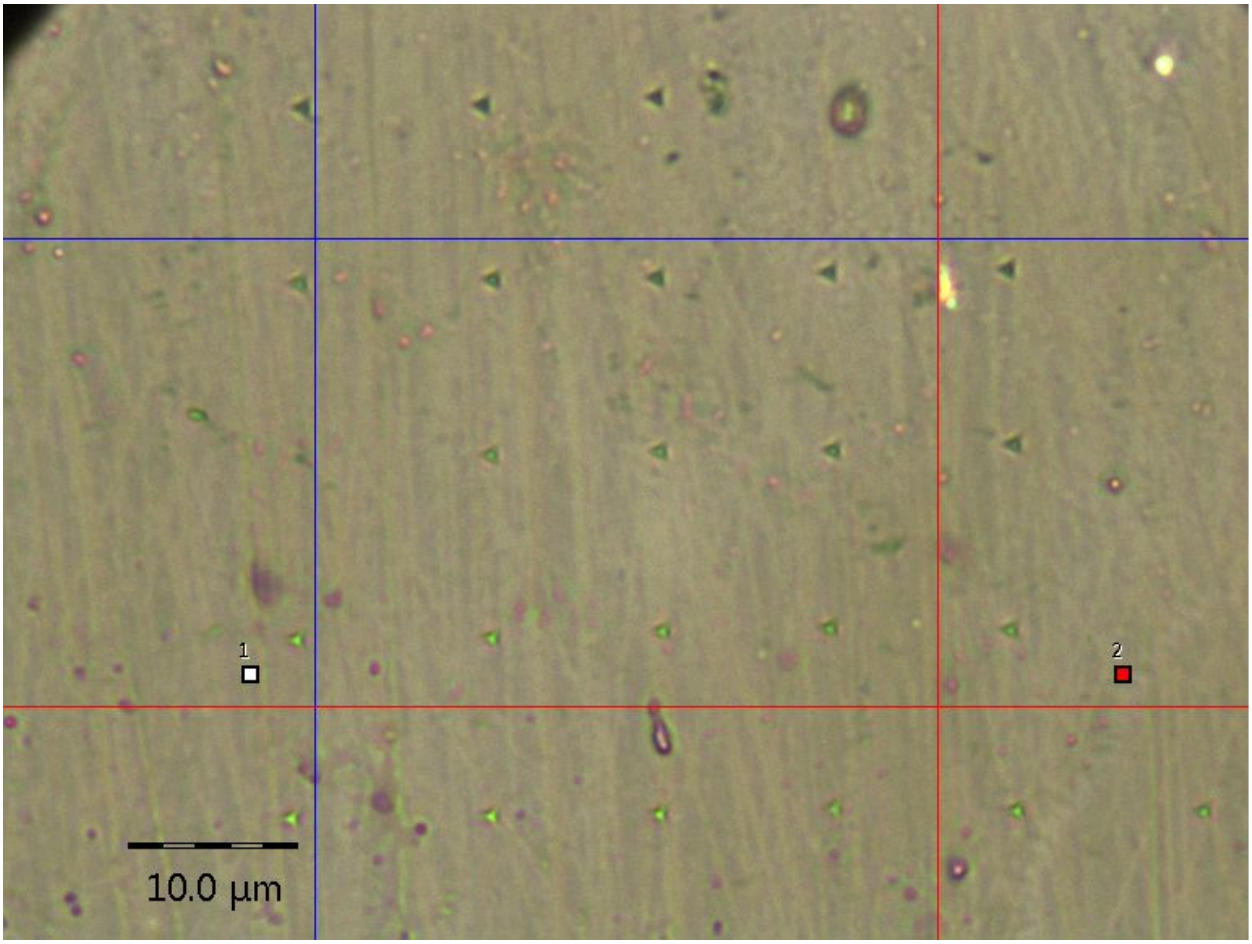

Figure 4.12: Nano-indentation grid after testing shown under microscope.

Each indent produced a force vs depth loading and unloading curve, as seen Figure 4.13. These curves are well-behaved, meaning that they approximate linear behavior, which indicates an accurate measurement [23]. Additionally, all of the curves are very similar, which is due to the homogeneous nature of the glassy material being tested.

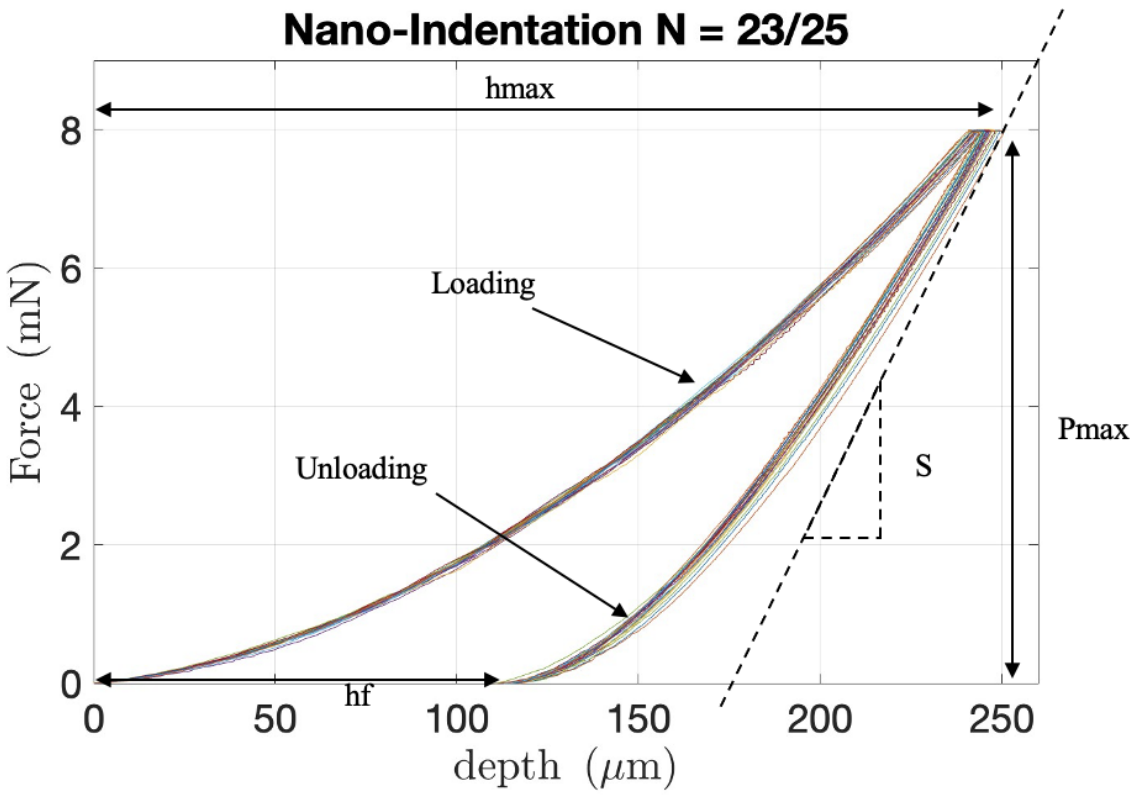

Figure 4.13: Nano-indentation testing resulting curves showing forces vs depth and the indentation characteristics derived from the curves

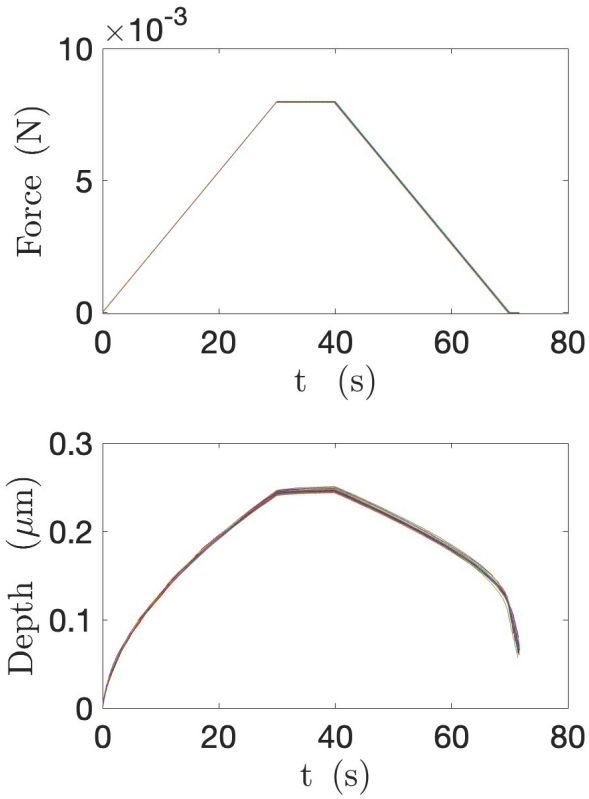

Figure 4.14: Nano-indentation force and depth vs time curves for all 23 indents in the first test

Using these curves and the Oliver and Pharr method ([19]) as described in Chapter 3.4, the average values for indentation hardness, indentation Youngs Modulus, and reduced Youngs Modulus of all indents were calculated.

Table 4.1: Final average values for first nano-indentation testing.

	H-IT (GPa)	E-IT (GPa)	Er (GPa)
Melt	8.1	77.1	78.9

4.2.2 Nano-indentation on a thin section of all three zones

The second test was a 976 indent grid on a thin section sample that was 12mm by 3mm in size. The grid consisted of 16 rows of 61 indents each. The approximate location of each

indent is indicated below by the dark blue dots.

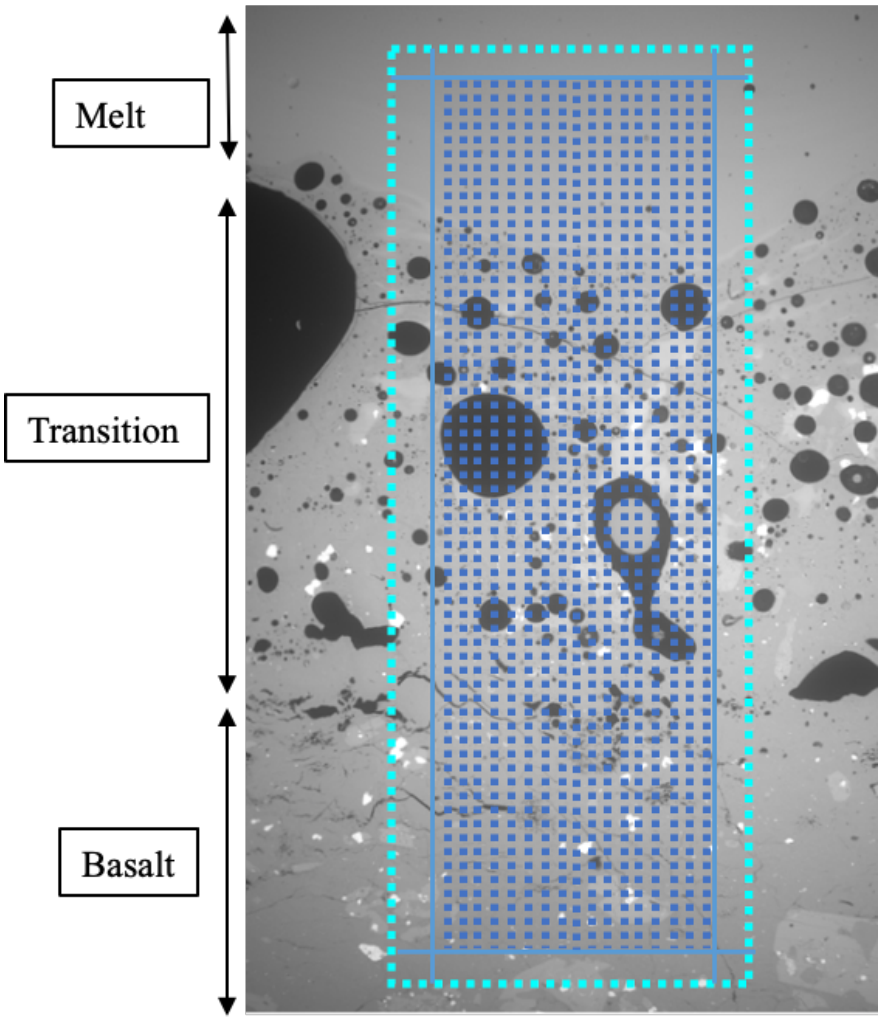

Figure 4.15: Schematic image showing the location of each indent that was planned.

Since these indent locations spanned over the entire sample, more points hit pores than in the previous sample (melted region only) and thus had to be removed in post processing. For each point, a loading/unloading curve was produced and for each loading/unloading curve the value of indentation hardness, indentation Young's Modulus, reduced Young's Modulus, and indentation creep were calculated. Indentation creep (C-IT) is the ratio of creep displacement during the holding stage to the maximum displacement during the loading stage

The data were post processed to remove outliers that were one standard deviation from

the mean since not well-behaved curves were present due to pores, and mechanical error. Additionally, for the indentation creep, negative points were removed. The results of this can be seen below. Each point corresponds to a different mechanical value calculated from the indent at that location. The color grid indicates the change in hardness and Young's modulus throughout the sample. Notice that there is more variation in hardness in the basalt region and then much more homogeneous values once we get to the melt. The transition section seems to have less variation than the basalt but still differences.

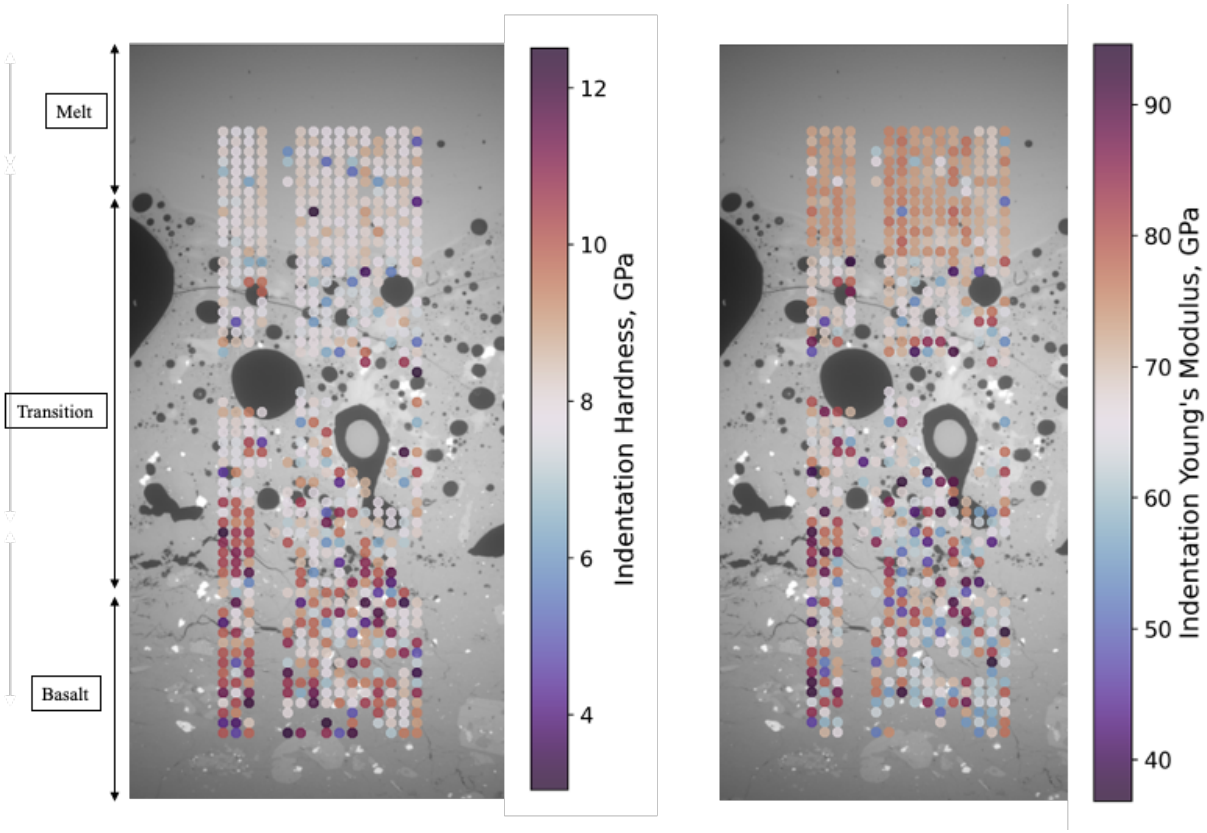

Figure 4.16: Resulting indentation hardness and indentation Young's Modulus color grid: each point corresponds to a successful indent

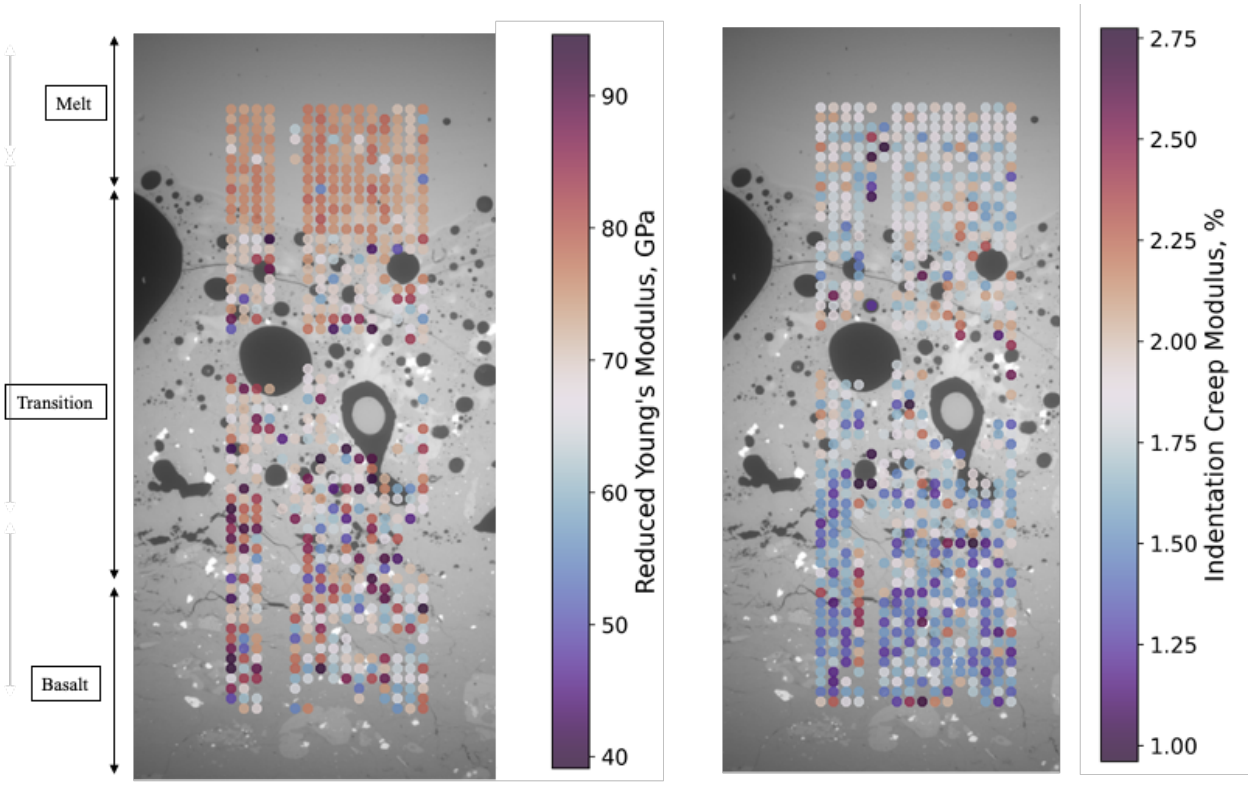

Figure 4.17: Resulting reduced Young's Modulus and indentation creep color grid: each point corresponds to a successful indent

Table 4.2 and Table 4.3 below show the average values and the standard deviations for each calculation in the different sections. Table 4.2 is with one standard deviation from the mean removed, which was used to make the images above. Table 4.3 shows the data without these values removed to get an understanding about the outliers that existed.

Table 4.2: Mean values and standard deviation with one standard deviation from the mean removed

	H-IT (GPa)	E-IT (GPa)	Er (GPa)
Melt	8.01 ± .60	72.93 ± 3.67	74.77 ± 3.92
Transition	7.98 ± 1.63	67.93 ± 11.24	69.89 ± 10.88
Basalt	9.18 ± 2.06	68.83 ± 12	70.83 ± 11.58

Table 4.3: Mean values and standard deviation with no data removal

	H-IT (GPa)	E-IT (GPa)	Er (GPa)
Melt	7.33 ± 2.52	67.86 ± 17.74	69.73 ± 17.82
Transition	6.93 ± 5.11	59.89 ± 31.79	61.34 ± 31.07
Basalt	8.76 ± 4.92	71.51 ± 31.10	72.72 ± 29.69

4.3 Raman Spectroscopy

Conducting Raman phase mapping involved the utilization of the confocal Raman microscope system (alpha300R, WITec, Ulm, Germany), see section 3.5 for more information. This system was equipped with a frequency-doubled Nd:YAG 532 nm laser, employed in conjunc-

tion with a multi-axis piezo scanner (P-527, Physik Instrumente, Karlsruhe, Germany), and a motorized large-area stage for precise sample positioning. During the scanning process, the system incorporated topographic data obtained through TrueSurface profilometry to sustain confocality in extensive area mapping. Raman spectra were captured using a thermoelectrically cooled CCD detector (DU401A-BV, Andor, UK), positioned behind the spectrometer (UHTS 300, WITec, Ulm, Germany), featuring a grating of 600 g $mm-1$. Each recorded Raman spectrum at a sample point had an integration time of 300 ms. At each pixel, three spectra were recorded and subsequently averaged. The measurement encompassed an area of 12000μm by 1800μm[24].

Both Raman mapping and point analysis was conducted. Raman mapping took points along the entire sample to produce a distribution map of the changing phases throughout the sample while in the point analysis specific locations were chosen and Raman specra were produced for these known points. Raman spectra are then plotted as Raman shift, which is the difference between the peak energies and the excitation laser energy[25].

The location of sampling was the same location on a thin section sample as the larger EDS test and larger nano-indentation test that were done. Figure 4.18 shows the exact location of the section used, which was 12mm in height and 1.8mm in width. This entire part included all three zones.

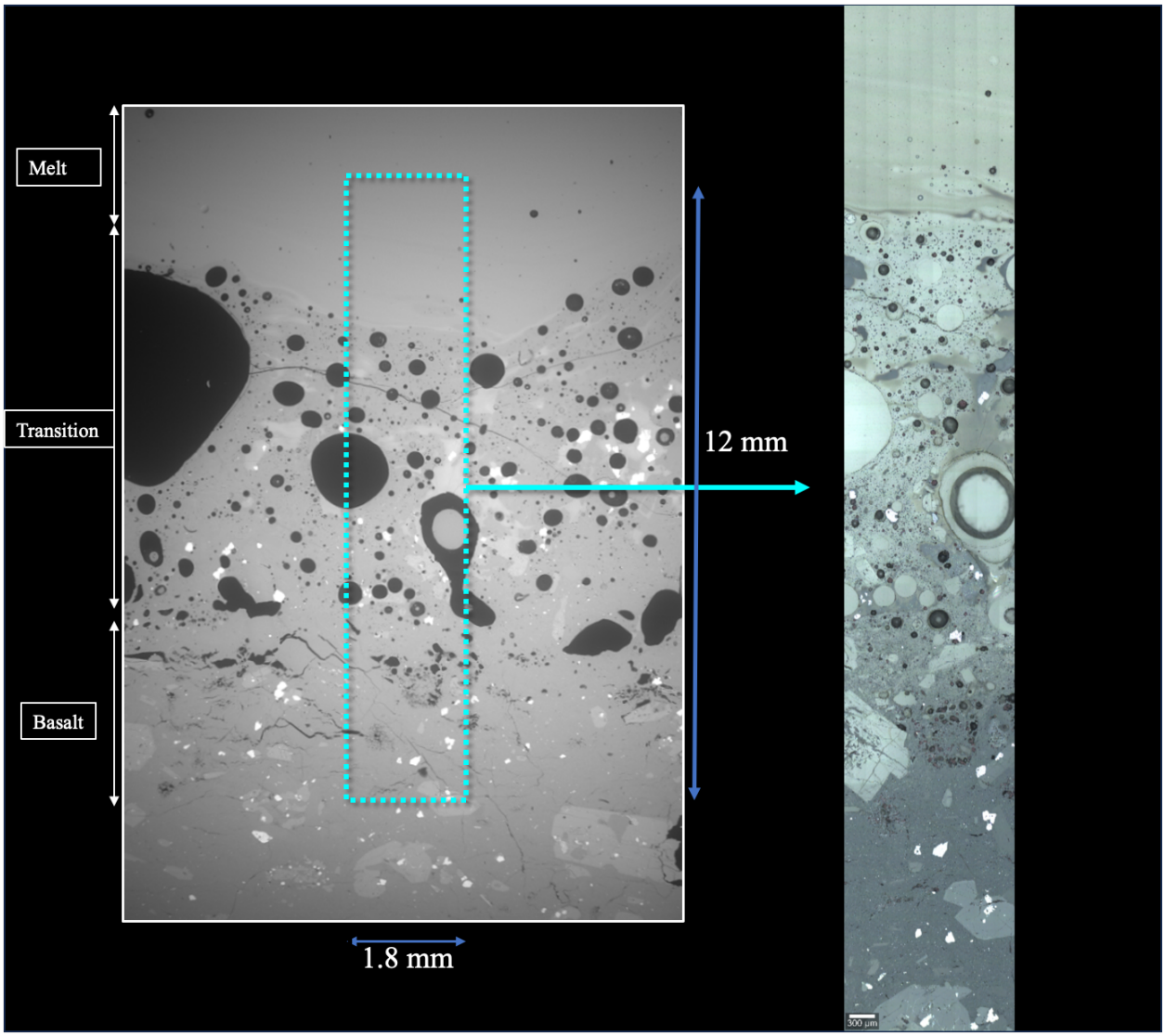

Figure 4.18: Optical image showing exact location on thin section sample where Raman testing was conducted.

The Raman mapping produced spectra that indicated different phases within the specimen. A color map indicating the changing phases is shown in Figure 4.19. Each color represents a different spectra and thus a change in composition and/or phase. As one can see in the lower part of the image (the non-melted basalt), some minerals are designated by varying colors. The yellow minerals have a spectrum that indicates the presence of magnesium, which was also confirmed in the EDS testing. Turquoise minerals indicate a high presence of aluminum, also verified by EDS.

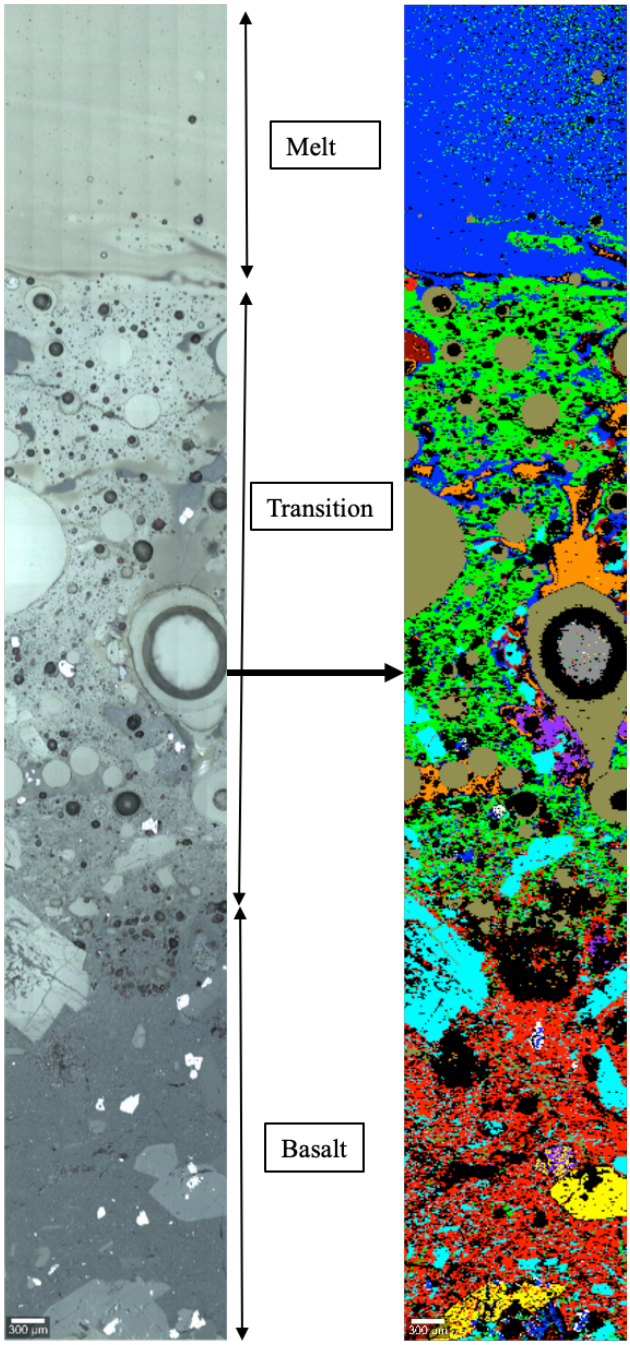

Figure 4.19: Color map produced from Raman testing of overall sample with each color indicating a change in Raman shift

The Raman mapping also indicated differences between the three different zones, as indicated by the change in color as one moves from Basalt to transition to melt (red to green to blue phase colors). These Raman shifts are then plotted and shown below. Notice the

similarities between the transition zone and the melted region as compared to the Basalt matrix. It seems as though, even though the transition was not directly exposed to MM-waves, it was still highly affected by the proximity to a high heat environment. This was also seen in the EDS testing. The raman peaks around 500 1/cm indicate the presence of SiO_2. However, at high temperatures, amorphous (non-crystalline) silica transitions into crystalline silica and thus we see this transformation as we move from basalt matrix to melted material.

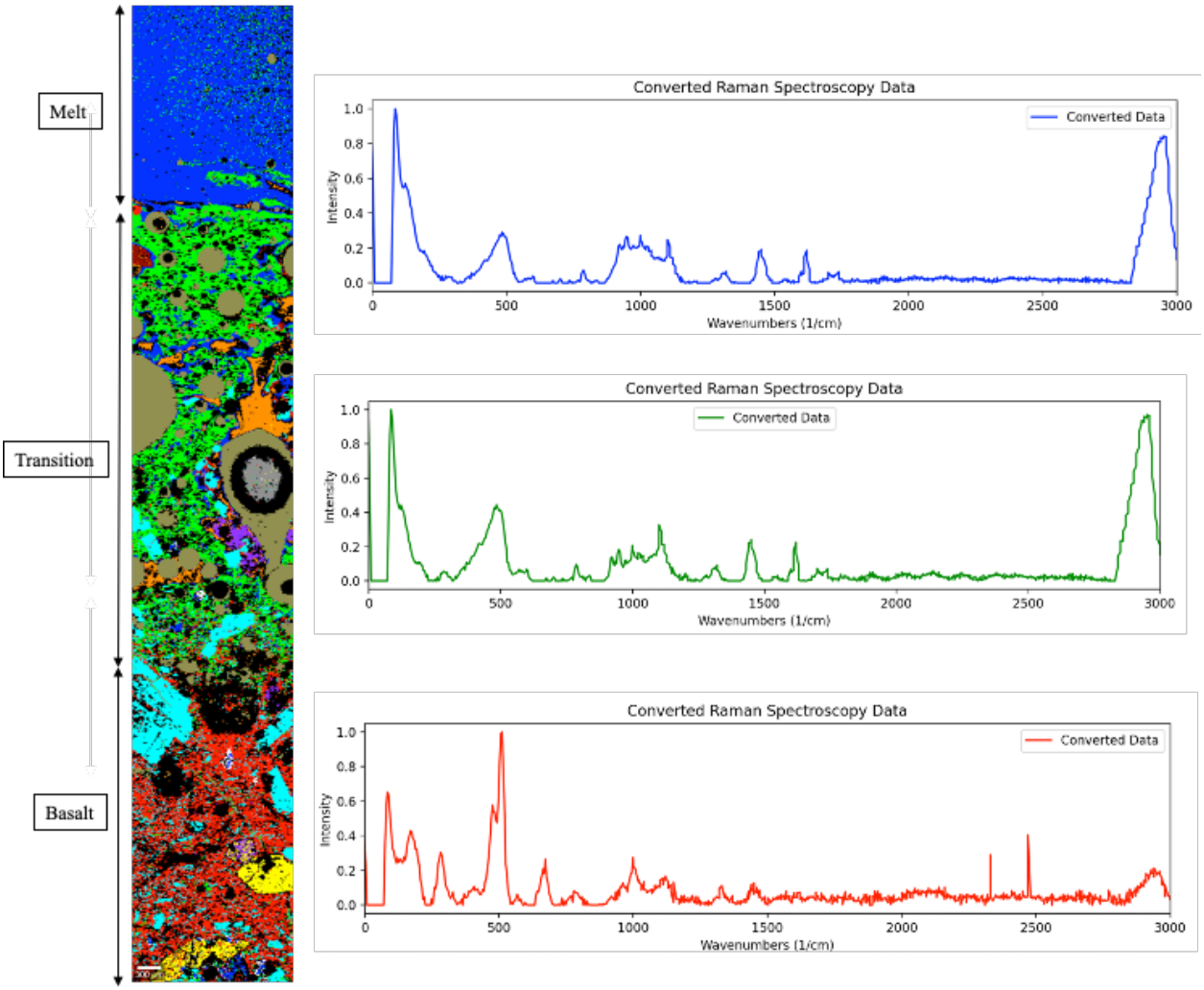

Figure 4.20: Raman map with Raman specra plotted for each Raman shift associated with the three different zones.

To understand these comparisons better, the Raman shifts for the melted region, the transition matrix, and pure soda lime glass were plotted below. Notice the similarities

between where the peaks for the pure glass are and the peaks for the melted region, thus indicating the transition from basalt to a partially silica glass.

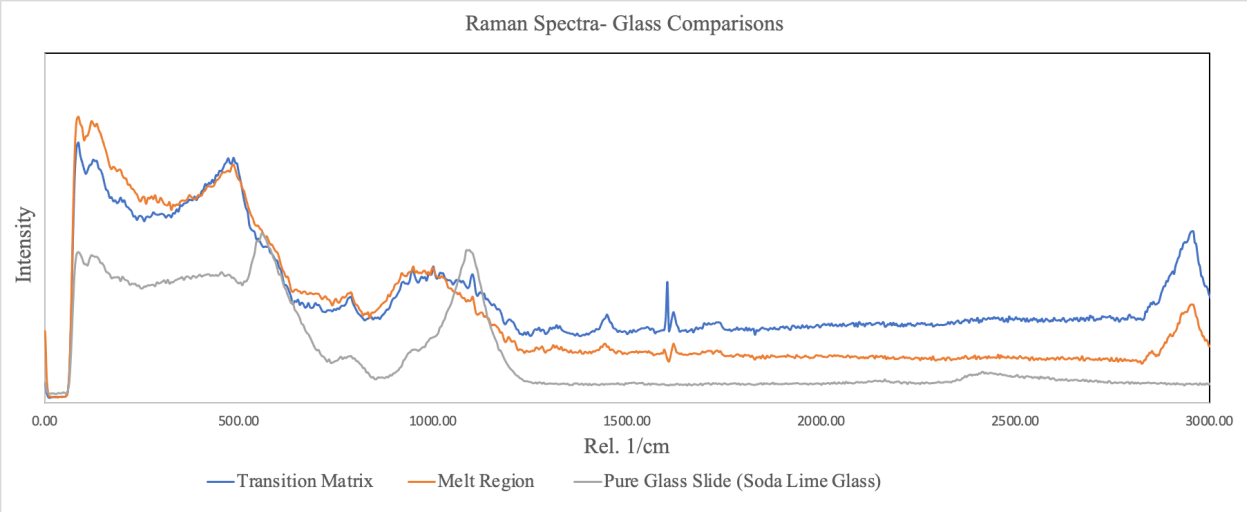

Figure 4.21: Raman specra for the transition matrix (blue), the melted region (orange), and pure soda lime glass (grey).

The main difference between all three spectra occurs between 880 1/cm to 1200 1/cm and this range is zoomed in on in Figure 4.22. This allows one to have a better understanding of the differences in the Raman spectra of the three zones. The red is again the melt, the blue is the transition matrix, and the green the basalt matrix. In Raman spectroscopy, the spectral range from 880 to 1120 1/cm corresponds to various vibrational modes associated with specific minerals and structural components in basalt and basalt glass. Amorphous or glassy phases in basalt can contribute to broad Raman bands in this region. The width and shape of these bands may vary based on the degree of glassiness and the specific glass composition, commonly associated with symmetric stretching vibrations of Si−O tetrahedra in silicate minerals, like pyroxenes and feldspars present in basalt. Different minerals may exhibit distinctive peaks within this range. These are most likely the causes for the slight differences in the spectra as the melt and the transition matrix both have glassy material but are exposed to different temperatures and thus different degrees of melting and cooling. This creates differences in the mineral phases and thus differences in Raman spectrum.

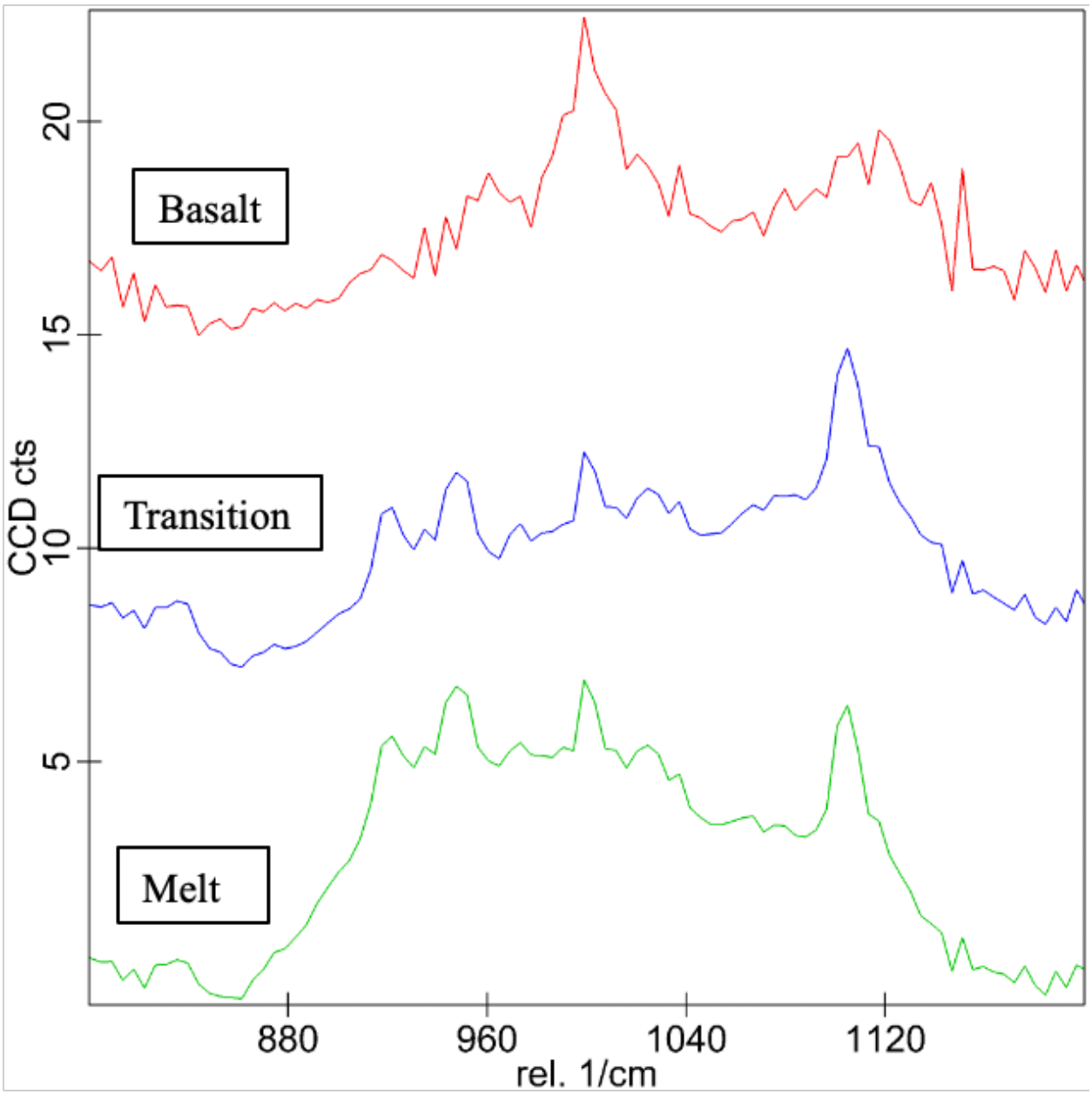

Figure 4.22: Zoomed in view of all three section differences.

The specra with a peak at 487 1/cm indicates just one of the Raman bands of SiO_2 -containing glasses. Specifically, a peak between 450-585 1/cm in a SiO_2 band, is attributed to the bending vibration (vb) or rocking of $Si-O-Si$ linkage [26]. A Gaussian curve was then fit to the peak at 487 1/cm and the intensity of this peak was plotted throughout the sample with the lightest color indicating high correlation to this peak and thus high intensity

of the SiO_2 glass. Figure 4.24 shows this intensity map. The melted region has the brightest color and thus it has the highest intensity of SiO_2 glas; The basalt then has the lowest and one can see the change from glass intensity moving from basalt to melted region.

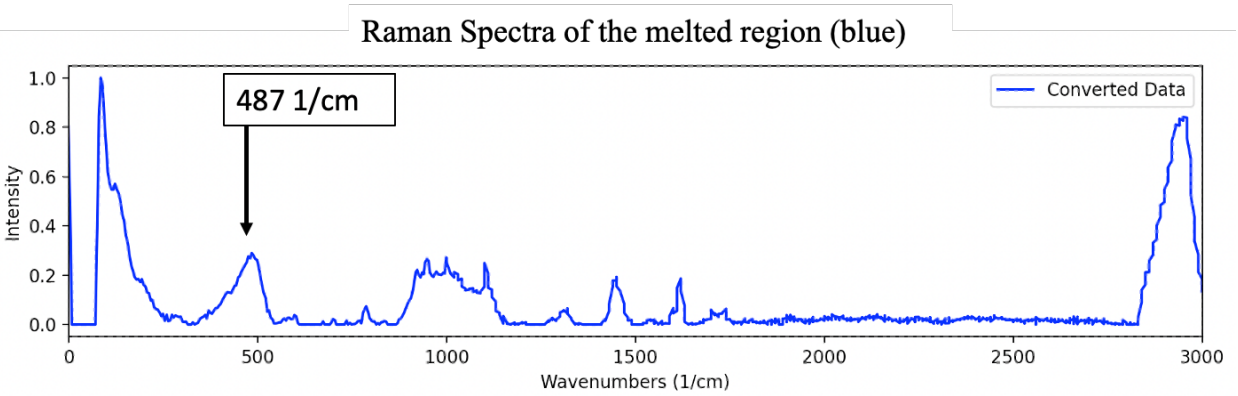

Figure 4.23: Raman shift of the melted region showing where the Gaussian curve was fit to.

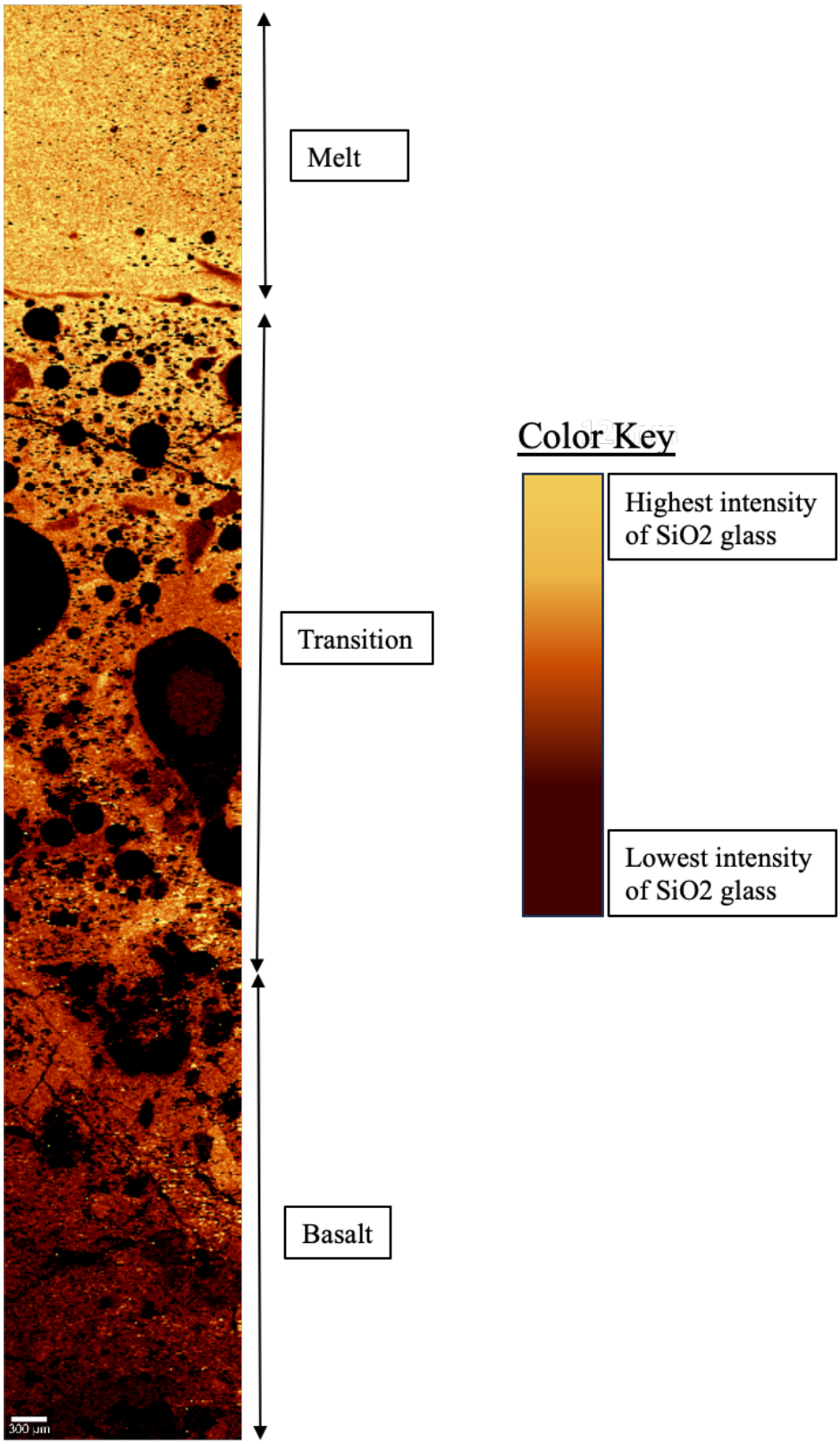

Figure 4.24: Raman Image showing intensity of glass material throughout specimen

Chapter 5

Conclusion

The research reported in the thesis was aimed at a major and a minor objective in the context of using mm-waves to create (drill and simultaneously case) deep wells in basement rock. The major objective was to interpret material properties in a mm-wave experiment in which hard basement rock was quickly melted and then solidified using mm-waves. Specifically, basalt encased in cement mortar to create 20cm diameter cylindrical samples was used. The results were then utilized in the minor objective to draw some inference on well stability.

The materiel properties of the original basalt, the transition between basalt and solidified melt, and the solidified melt were investigated with SEM-EDS, Nano-indentation, Raman Spectroscopy, and optical imagery. These investigations led to the following results:

- The melting of basalt rock with MM-waves creates a vitrified melt material that is a non-crystalline amorphous solid.
  -This vitrified material is made primarily of silica (SiO_2) and aluminum oxide (Al_2O_3) with smaller amounts of iron oxides (FeO, Fe_2O_3).

- Observed through scanning electron microscopy (SEM), the occurrence of micro-cracking in the basalt and melt materials is attributed to rapid temperature fluctuations. This phenomenon is a result of the minerals expanding when the rock undergoes heating,

exerting pressure on the adjacent rock and ultimately giving rise to the formation of microcracks, which have the potential to expand over time.

- Based on SEM-EDS testing and optical imagery we know the basalt has pyroxene, plagioclase, and olivine crystals.

- Based on the Raman experiments, there is a clear change of phase between the basalt matrix, the transition and the melt. The melt is mostly pure glassy material while the transitions matrix chemical composition and molecular structure is closer to that of the melted region than of the basalt.

- We see the partial melting of minerals within the transition zone, specifically that of olivine.

  - Additionally, there are phase changes within the molecular structure of the minerals when going from the basalt region to the transition zone.

- The glass material is stronger than that of silicon glass [19].

- The basalt has higher hardness values than both the transition zone and melt. However, the Youngs Modulus of the melt is the highest. Overall, the transition zone has the lowest strength values throughout the sample.

- Initial inferences regarding wellbore stability are:

  -Microcracking can weaken the overall strength of a wellbore, as it can lead to the formation of larger fractures and the potential for the wellbore to collapse. The presence of microcracks can also make the wellbore more susceptible to fluid migration, which can compromise the integrity of the well and lead to leaks or other environmental hazards [27].

  -Due to the variability of the transition zone's chemical make-up and lower mechanical strength values it would pose as a significant risk to wellbore stability. If there are ways

to minimize the transition zones thickness when using MM-waves to drill it would be ideal as it seems to significantly weaken the surrounding rock.

5.1 Future Work

These experiments and analyses are just a small part of what can be done in terms of understanding the material created by MM-waves and its usage. This work identified several topics of interest that could be further studied:

- Raman spectroscopy can provide very valuable in-depth insight into what is really happening to the rock pre- and post-melting. The analysis done in this thesis only covers the surface of what could be looked at. It would be interesting to understand how the actual molecular structures are changing in each mineral present and what the structure of the melt really looks like.

- Preliminary triaxial loading, heat capacity, and thermal conductivity tests have already been conducted on the basalt pre-melt and so when larger melted samples are available, triaxial loading tests can be done to compare these strength values to give insight into larger scale properties.

- The exact temperature at which these samples were melted is unknown. However, with an expected development in the MM-wave technology these values will be much more precise, which will in turn help data analysis. This is because the quality of the basalt melt is very much dependent on the mineral components and melting properties. These include the initial liquid temperature, melting temperature, melting process, and homogeneity of the melt [14].

- Focusing on the thermodynamics and how these play a role in the rapid heating and cooling of basalt would be vital in understanding the processes at play.

- Trying to understand other possible uses of this mm-wave vitrification process and material would be valuable. For example, using mm-waves for mineral/elemental extraction could be one avenue as we were seeing elemental changes and the possibility of iron being pulled to the surface of the melted sample.

Appendix A

Appendix A

Millimeter Wave Project Pre-Exposure Test Summary-Lyons Sandstone

A.1 Introduction

This report describes the mechanical and thermal properties of Lyons Sandstone before vitrification. A triaxial test was conducted in addition to heat capacity and thermal conductivity testing. These results and preparation are detailed below.

A.2 Triaxial Unloading Test

In this research, one triaxial unloading test was conducted on the sandstone. The tests was done using the NER AutoLab 3000 triaxial cell that is in the MIT Department of Earth, Atmospheric, and Planetary Sciences Rock Mechanics Laboratory.

For this test, the cylindrical specimen was kept under dry conditions (i.e. no pore pressure). The specimen size is detailed in the table below.

Table A.1: Specimen Size and Mass

Height	2.9 inches
Diameter	1.54 inches
Mass	213.6 grams

The preparation process included first coring and polishing the rock specimen. The cylindrical specimen was cored from a sandstone block using a water core drill. Figure A.1 shows the coring machine that was used.

Figure A.1: Coring machine used with water as coring liquid

After coring, the specimen needed to be polished and paralleled. A grinder, as show in in Figure A.2, was used to polish and parallel the top and bottom surfaces and a lathe (Figure A.3) was used to polish the lateral surface.

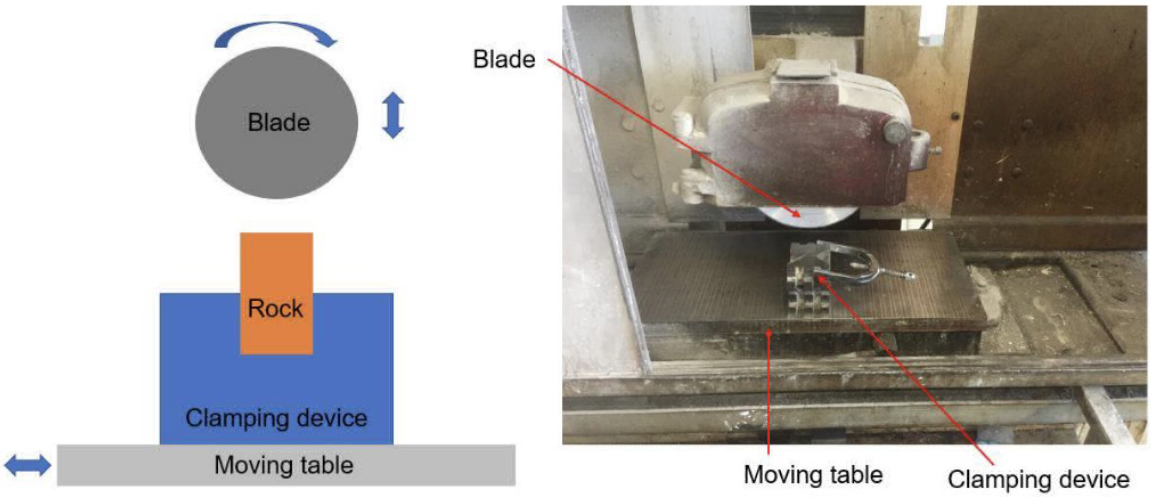

Figure A.2: Schematic showing the flattening and polishing of the two ends of the specimen ([28]).

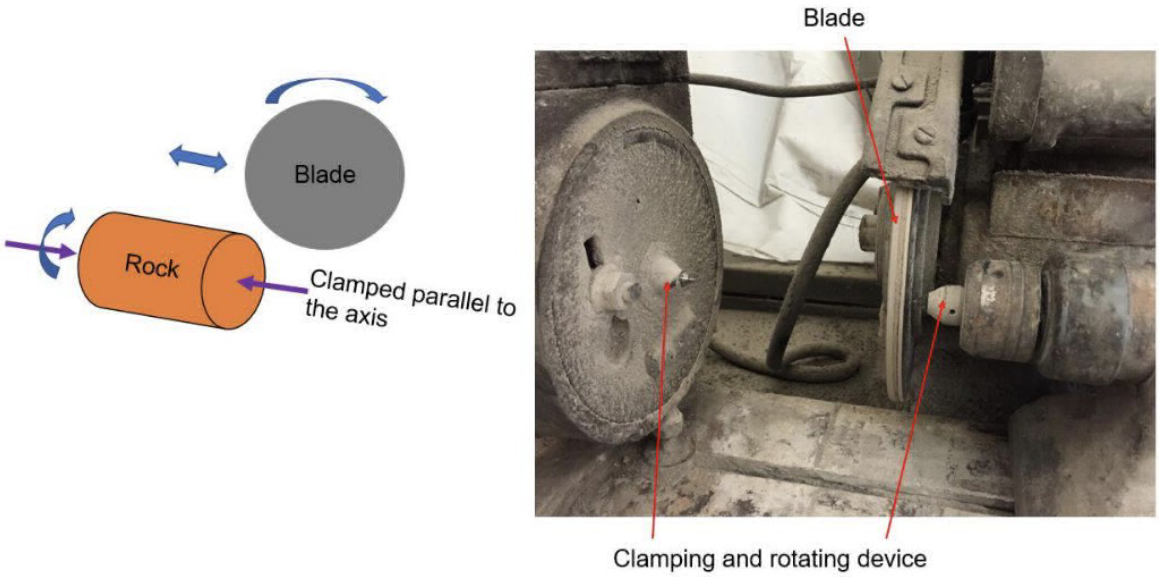

Figure A.3: Schematic showing the lateral surface polisher ([28])

After the coring and polishing processes, the specimen was sealed using a copper jacket that was attached to the circumferential surface and then soldered on. Next, two Viton tubes were cut and used as seals for the specimen.

The specimen was then placed inside a confining vessel with a pressure of 10 MPa to firmly attach the copper jacket to the specimen to prevent leakage during testing.

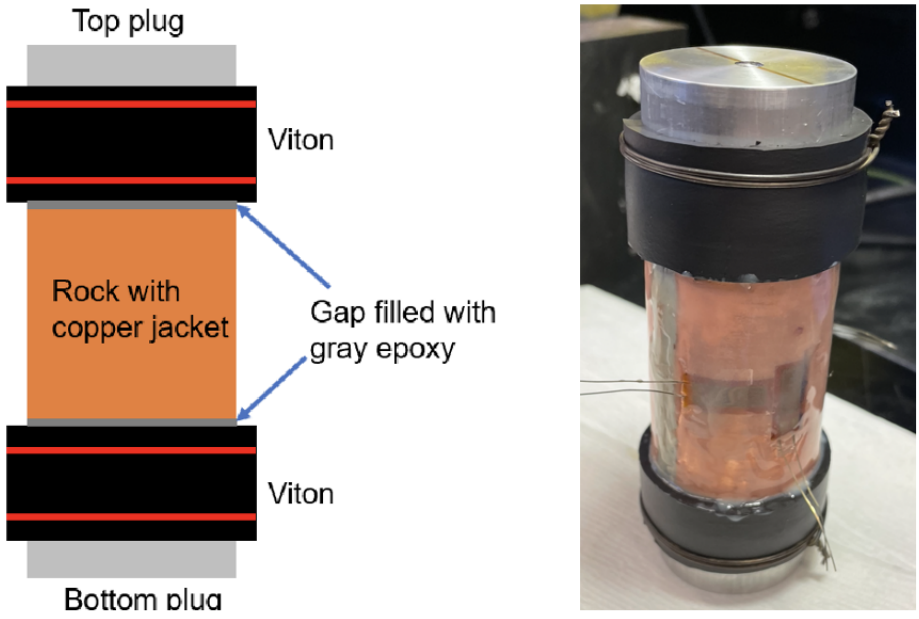

Figure A.4: Sealing of the specimen. A wire is used to secure the Viton tubes to the specimen.

Two axial strain gauges were glued onto the copper jacket with a 180 degree separation. Figure A.5 shows the location of these strain gauges.

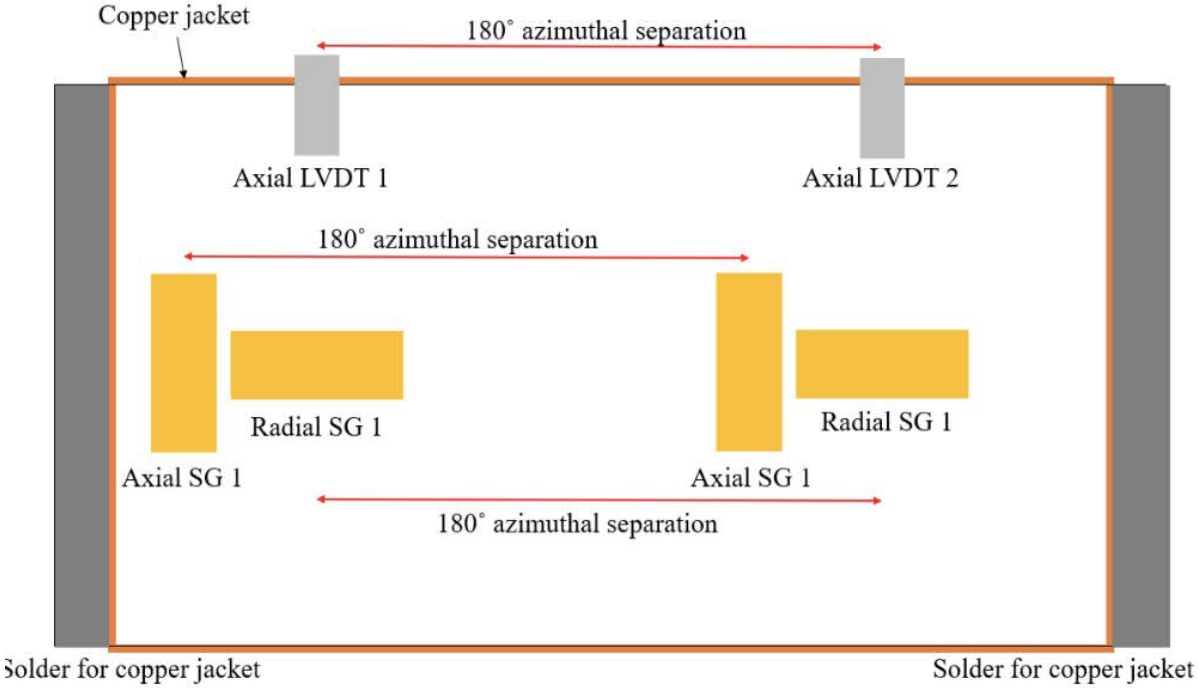

Figure A.5: Location of axial and radial strain gauges.

After this preparation, the specimen was placed inside the triaxial cell (Figure A.6).

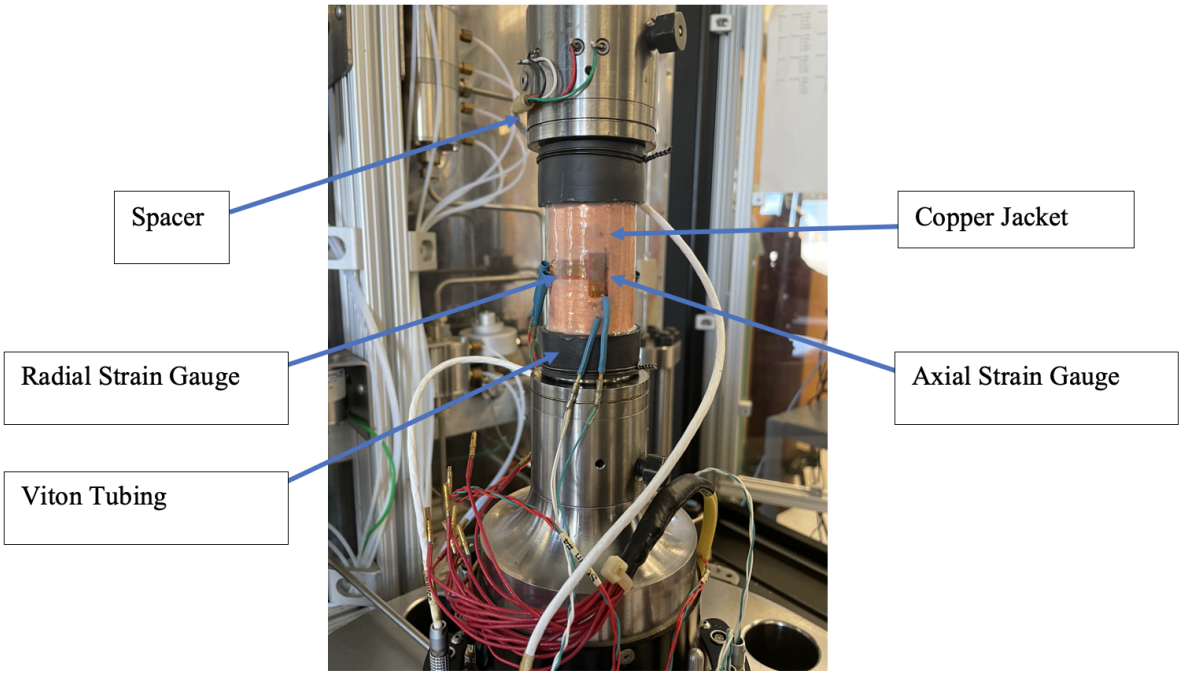

Figure A.6: Location of axial and radial strain gauges.

During the testing, multiple steps were applied to the specimen. Tables A.2 and A.3 summarize these stress steps. Table A.2 was the first part of this test that included loading the confining pressure up to 60 MPa while keeping the differential stress constant. This was to get moduli values for the specimen. Table A.3 then lists the steps in the second part of this test which involved starting both confining and differential at 5 MPa then doing an unloading stage and a creep stage.

An unloading test was done because the unloading process occurs during excavation of a well-bore or tunnel which is the case in this project.

Table A.2: Part 1 of the triaxial test

Part 1			
	Confining Pressure (Mpa)	**Differential Stress (Mpa)**	**Axial Stress (=CP+DS)**
Step 1	20	20	40
Step 2	40	20	60
Step 3	60	20	80

Table A.3: Part 2 of the triaxial test

Part 2				
	Confining Pressure MPa	**Differential Stress MPa (load)**	**Axial Stress (=CP+DS)**	Notes
Step 1	5	5	10	
Step 2	105	10	115	
Step 3	5	110	115	Held 24 hour for creep
step 4	60	20	80	
Step 5	40	20	60	
Step 6	20	20	40	
Step 7	5	0	5	

Figure A.7 shows the stress-strain curves of moving from step 1 to step 2. The specimen is being compressed uniformly. The axial and radial strain were both measured using the axial and radial strain gauges. The volumetric strain was then calculated as:

$$\text{Volumetric strain} = \text{Axial strain} + 2* \text{ Radial strain}$$

Increased confining pressure from 5 to 105 MPa and axial stress increased from 10 MPa to 115 MPa (differential stress increased from 5 to 10 MPa):

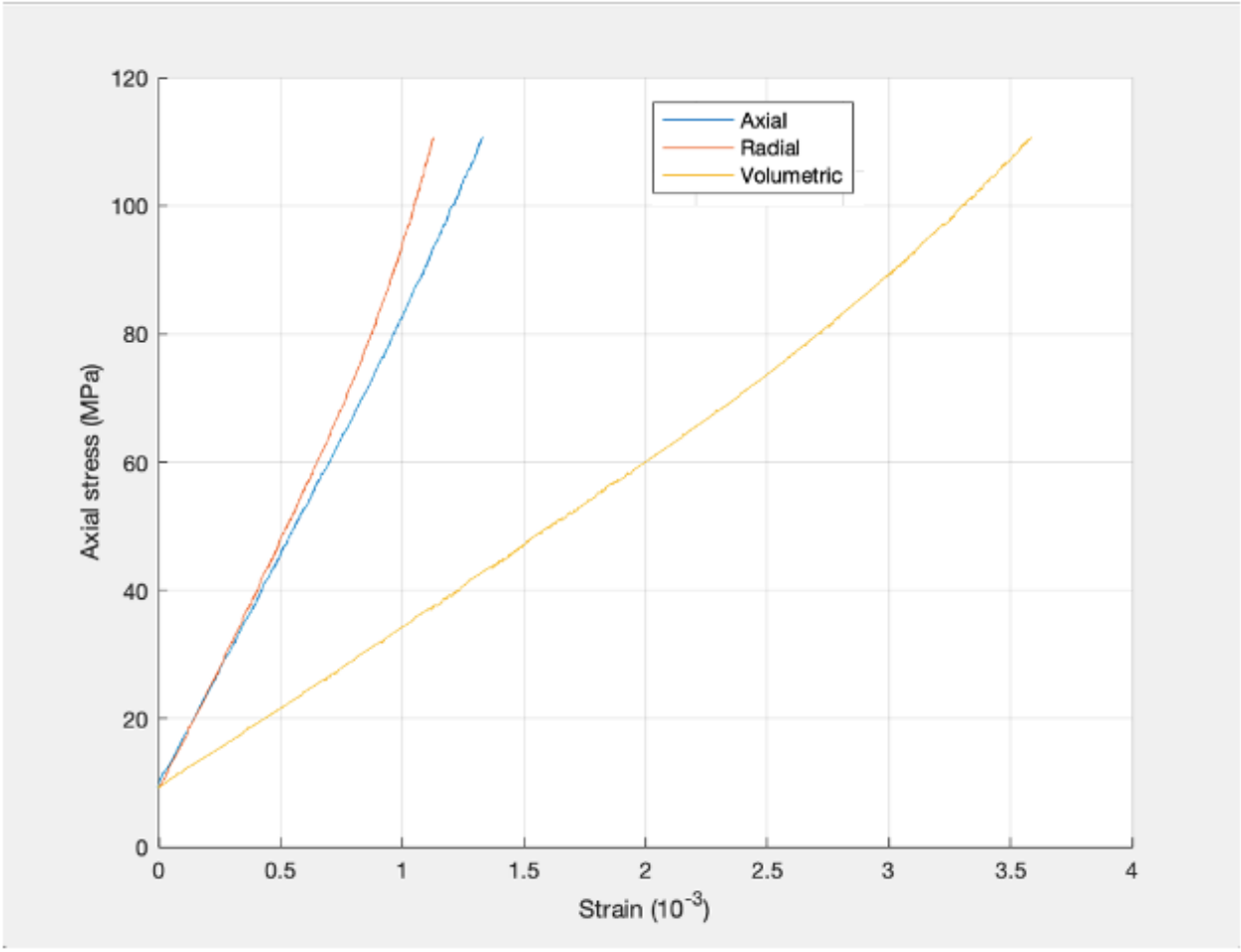

Figure A.7: Axial, Radial, and Volumetric strain vs the Axial Stress when increasing confining pressure to 105 MPa and axial stress to 115 MPa.

Figure A.8 shows the stress-strain curve for moving from step 2 to step 3. This involves unloading the specimen. The axial stress is kept at 115 MPa and the confining pressure is decreased to 5 MPa.

Decreased confining pressure from 105 to 5 MPa and kept axial stress at 115 (increased differential stress from 10 to 110)

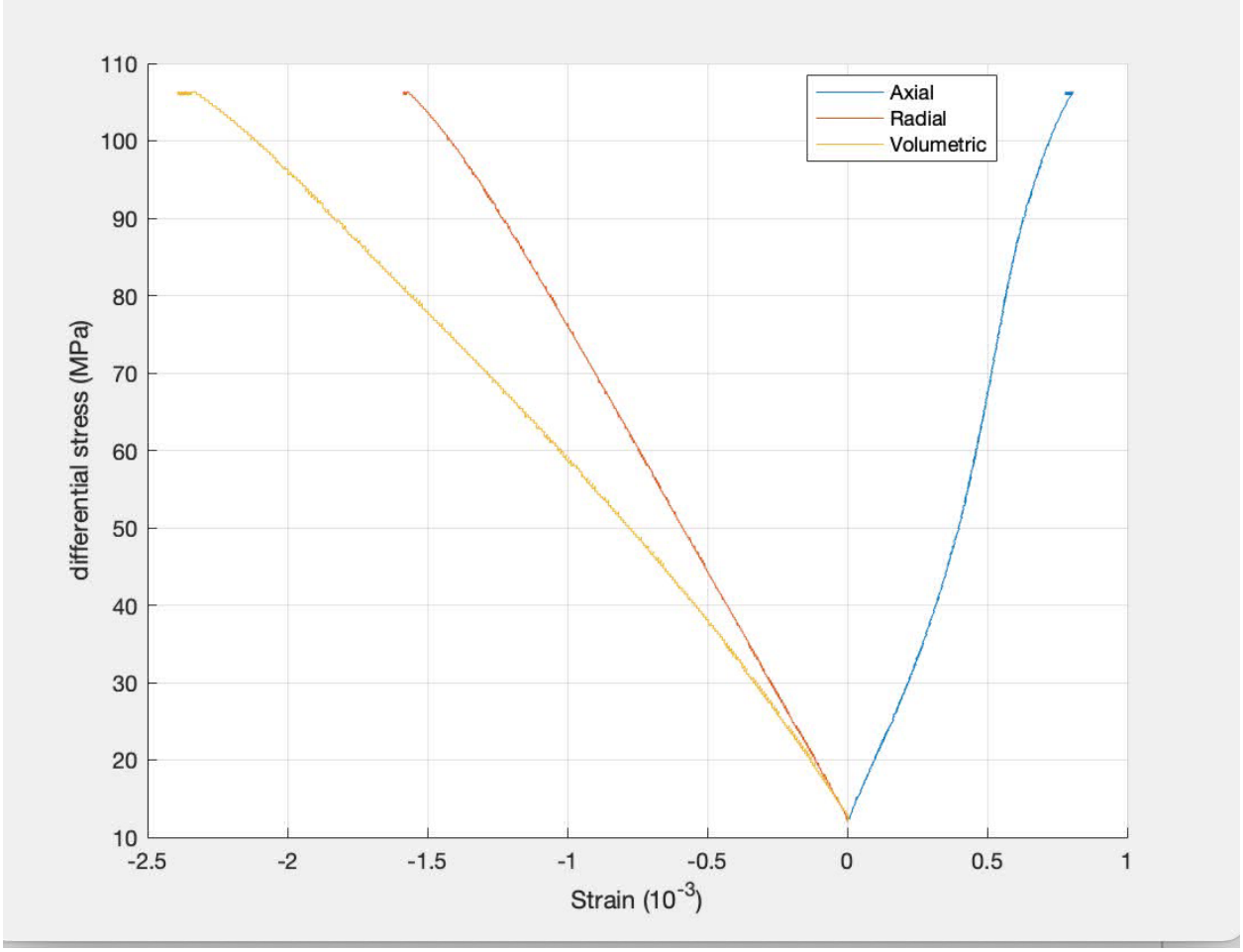

Figure A.8: Showing the axial, radial, and volumetric strain vs differential stress (AP-CP) for when confining pressure is decreased to 5 MPa and axial stress is kept at 115 MPa.

The axial and confining pressures were then fixed at these values and creep deformation was measured. The specimen was held at a confining pressure of 5 MPa and an axial stress of 115 MPa for 24 hours. Figure A.9 shows the axial and radial strain changing with time over the 24 hour time period.

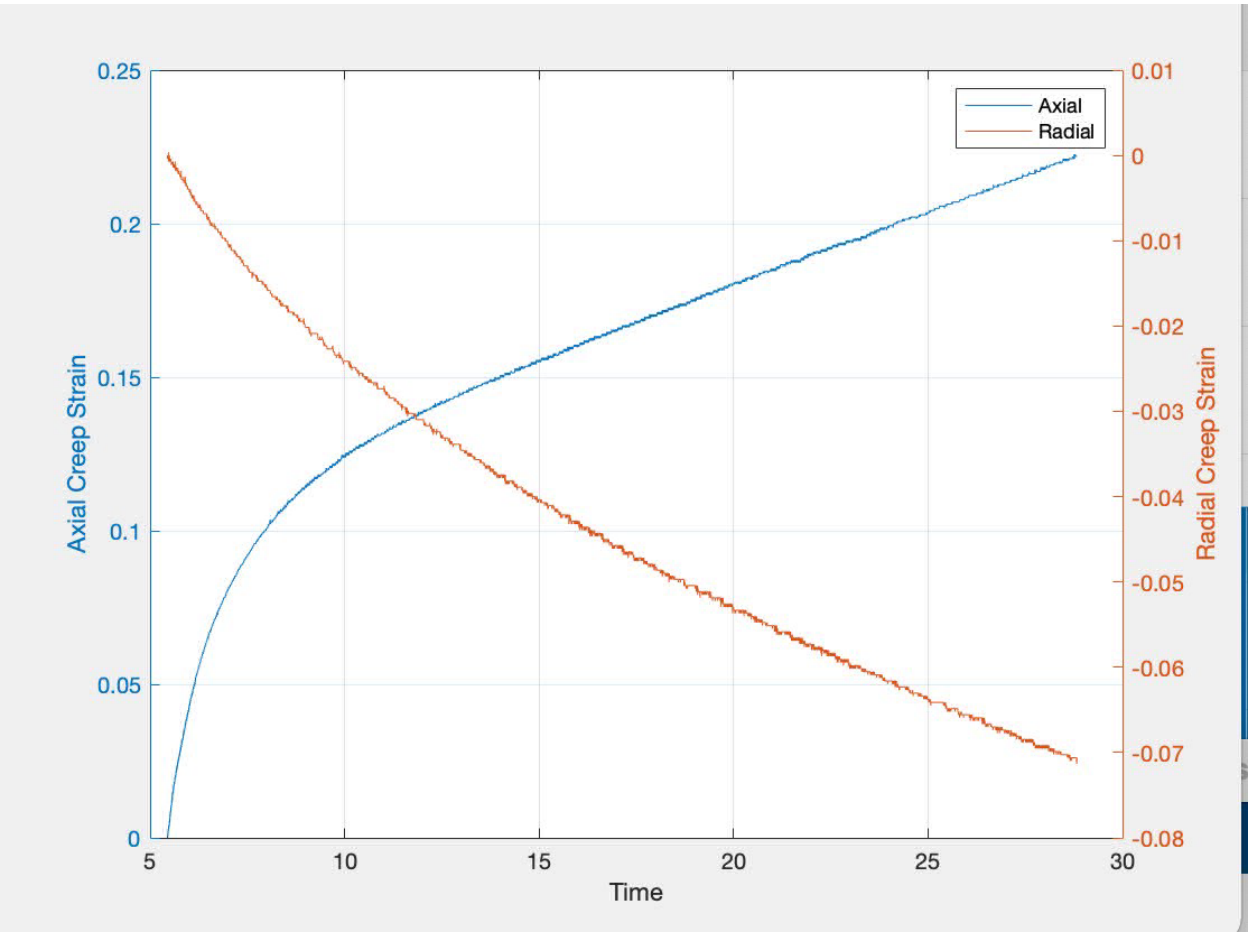

Figure A.9: Axial and radial creep strain versus time for a 24 hour period. Hour 5 is when the creep test began.

After the creep deformation the specimen was unloaded again. This unloading was done in stages. Fist, the axial stress was decreased from 110 to 80 MPa, then to 60MPa, then to 40MPa, and finally to 5 MPa while the differential stress was decreased to 20 MPa and held constant during unloading.

Figure A.10 shows the stress-strain curve for moving from step 3 to step 4. The axial stress is decreased to 80 MPa and the confining pressure is increased to 60 MPa (differential stress decreases from 110 MPa to 20 MPa)

Increase confining pressure to 60 and decrease axial stress to 80 MPa

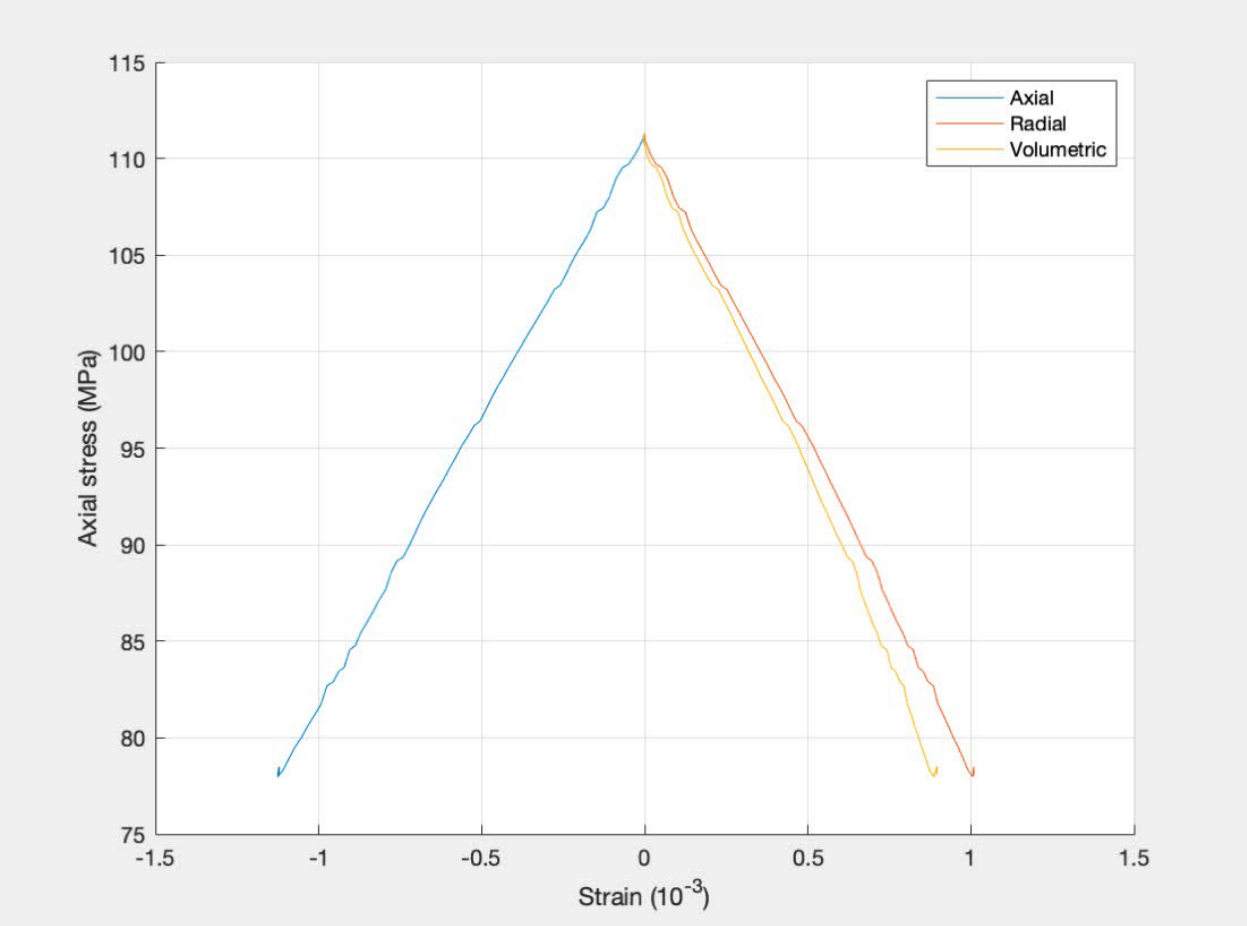

Figure A.10: Showing the axial, radial, and volumetric strain vs axial stress for when axial stress is decreased to 80 MPa.

As described above, the specimen was unloaded in stages. This shows the final stage when decreasing the axial stress from 40 MPa to 15 MPa

Figure A.11 shows the stress-strain curve for moving from step 6 to step 7. This involved decreasing the differential stress to 10 MPa and decreasing the confining pressure to 5 MPa. (Axial stress is decreased from 40 MPa to 15 MPa)

Decrease confining pressure to 5 MPa and decrease axial stress to 15 MPa

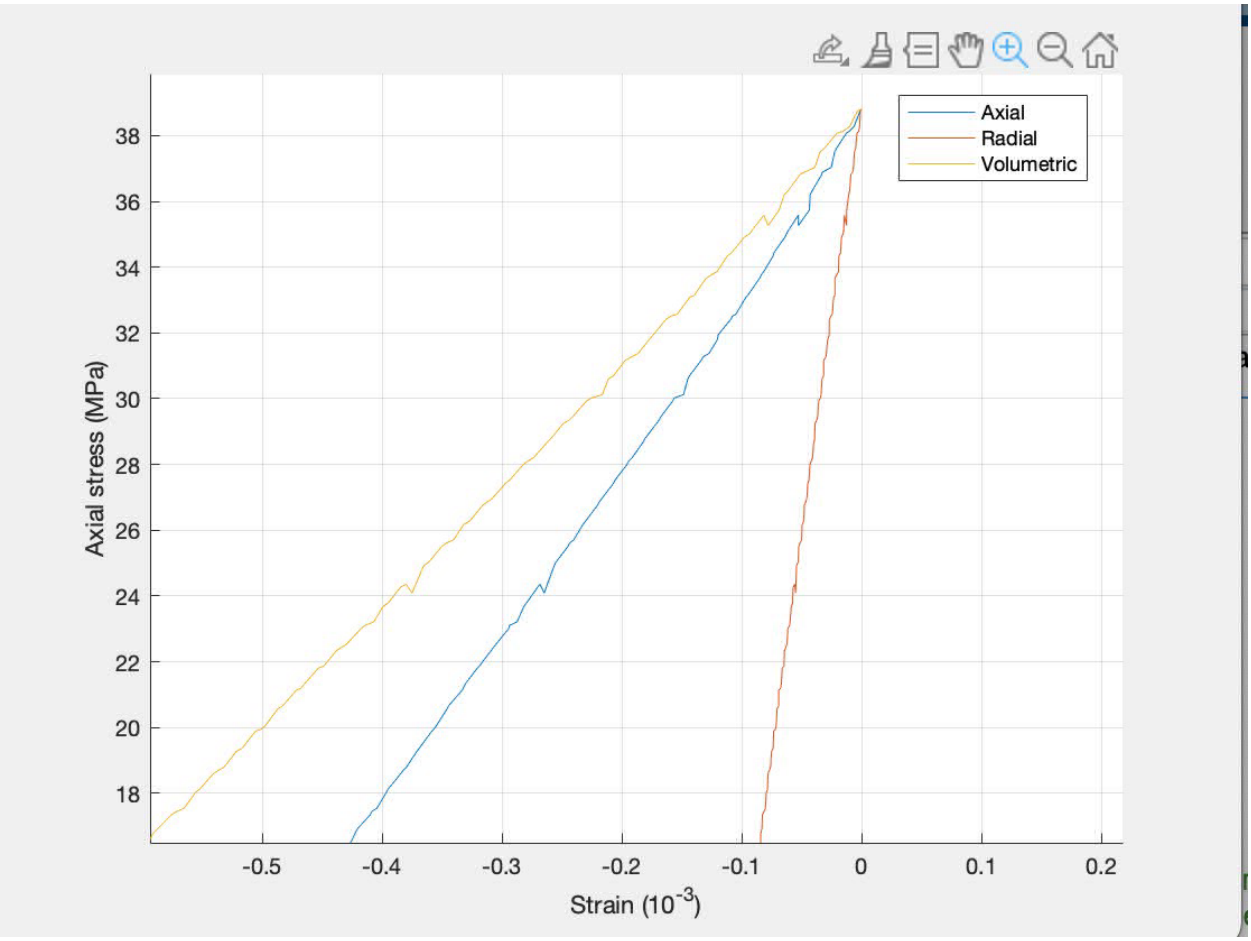

Figure A.11: Showing the axial, radial, and volumetric strain vs axial stress for when confining pressure is decreased to 5 MPa and axial stress is decreased to 15 MPa.

The elastic modulus (E), Poisson's ratio (v), shear modulus, and bulk modulus were calculated at confining pressures of 20 MPa and 40 MPa. They were calculated based on the measured axial strain and radial strain values where sigma 1 is the axial stress and sigma 3 is the confining pressure.

$$\varepsilon_{axi} = \frac{1}{E}\left[\sigma_1 - v\left(\sigma_3 + \sigma_3\right)\right]$$
$$\varepsilon_{rad} = \frac{1}{E}\left[\sigma_3 - v\left(\sigma_1 + \sigma_3\right)\right]$$

Table A.4: Moduli and Poisson's ratio

Confining Pressure (MPa)	Differential Stress (MPa)	Youngs Modulus (GPa)	Poissons Ratio	Bulk Modulus (GPa)	Shear Modulus (GPa)
20.18	18.93	46.6	0.097	25.87	20.12
40.11	18.56	48.2135	0.103	25.67	21.28

A.3 Specific Heat Capacity Measurements

The specific heat capacity of the sandstone was measured using a differential scanning calorimeter at the MIT Institute for Soldier Nanotechnologies.

To prepare the specimen for this test, the rock was ground into a fine powder. First, the specimen was crushed into small pieces with a hammer. Then, the small pieces were ground into a fine powder using a soil mortar and porcelain pestle (produced by the Gilson Company), and the powders passed through the number 200 sieve (grain size finer than 75 μm). For each measurement, approx. 10 mg of powders was required.

The specific heat capacity, c_p (J / (g$*$ °C)), is calculated as follows, where m is the mass (g), ΔQ is the heat change, and ΔT is the temperature change (C). °C

$$c_p = \frac{\Delta Q}{m\Delta T}$$

The test was done at a temperature increasing rate of 20 °C/min and taken from 50 °C to 400 °C. Figure A.12 indicates the specific heat capacity at different temperatures.

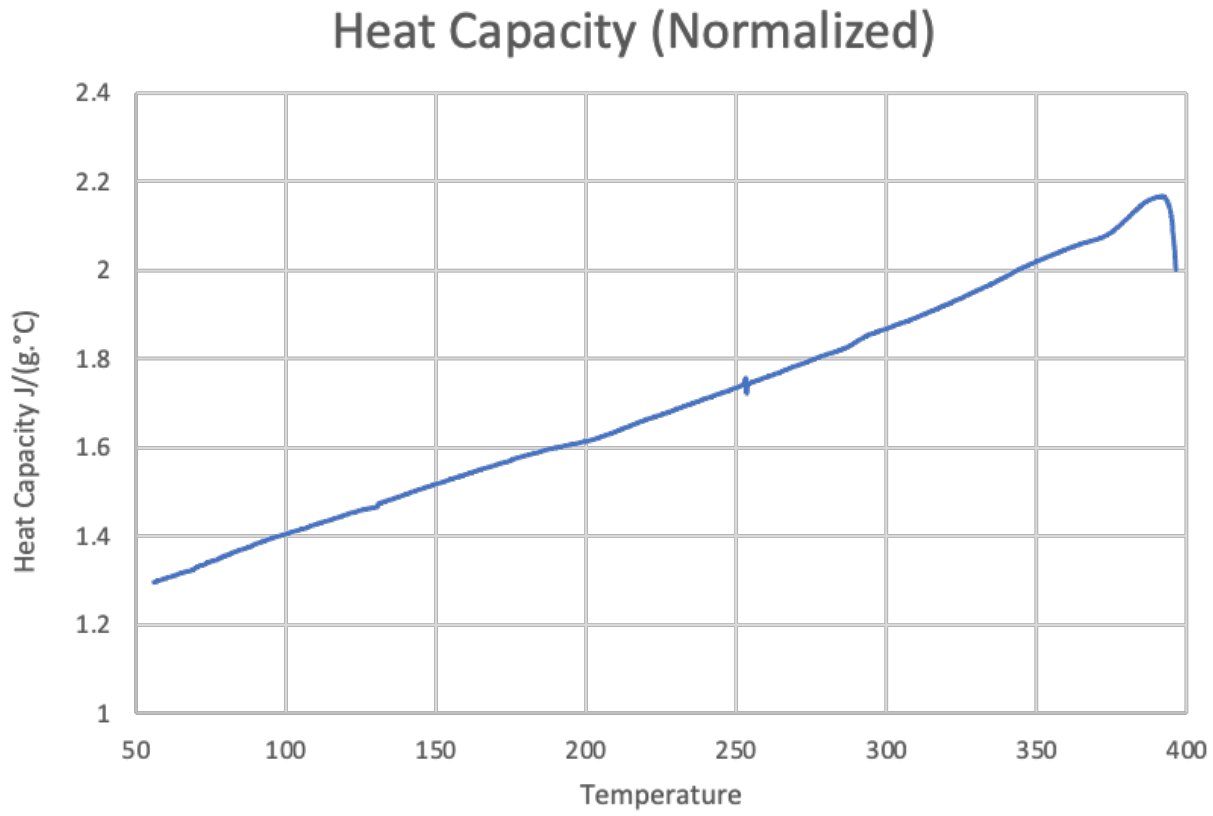

Figure A.12: Heat capacity versus temperature for the sandstone specimen.

Next, the volumetric heat capacity was measured and was found to be around 2MJ/m^3 K. The volumetric heat capacity of a certain material is the heat capacity of the specimen divided by the volume of that specimen. It is the amount of energy that must be added to one unit of volume of the material in order to cause an increase of one unit in its temperature.

A.4 Thermal Conductivity Measurements

The thermal conductivity of the sandstone specimen was measured using a steady-state thermal conductivity device through the MIT Nano Engineering Group.

The specimen preparation for this included cutting the sandstone into a block 2cm by 2cm by 2cm then polishing the faces with silicon carbide grinding paper.

The results showed that the thermal conductivity was in the range of 5-9 W/m K and that the in-plane and cross-plane thermal conductivities are also somewhat different at different locations. This is consistent with known thermal conductivity of quartz, which is anisotropic and varies from 5-10 W/m K depending on the crystal orientation.

Figure A.13 shows a picture of the whole specimen face and the colored box indicates the location on this surface that the testing was done. Figure A.14 then shows an up-close view of this specific location and the thermal conductivities at each specific point. Figure A.15 is a contour plot of the surface of this location where the testing was taken place

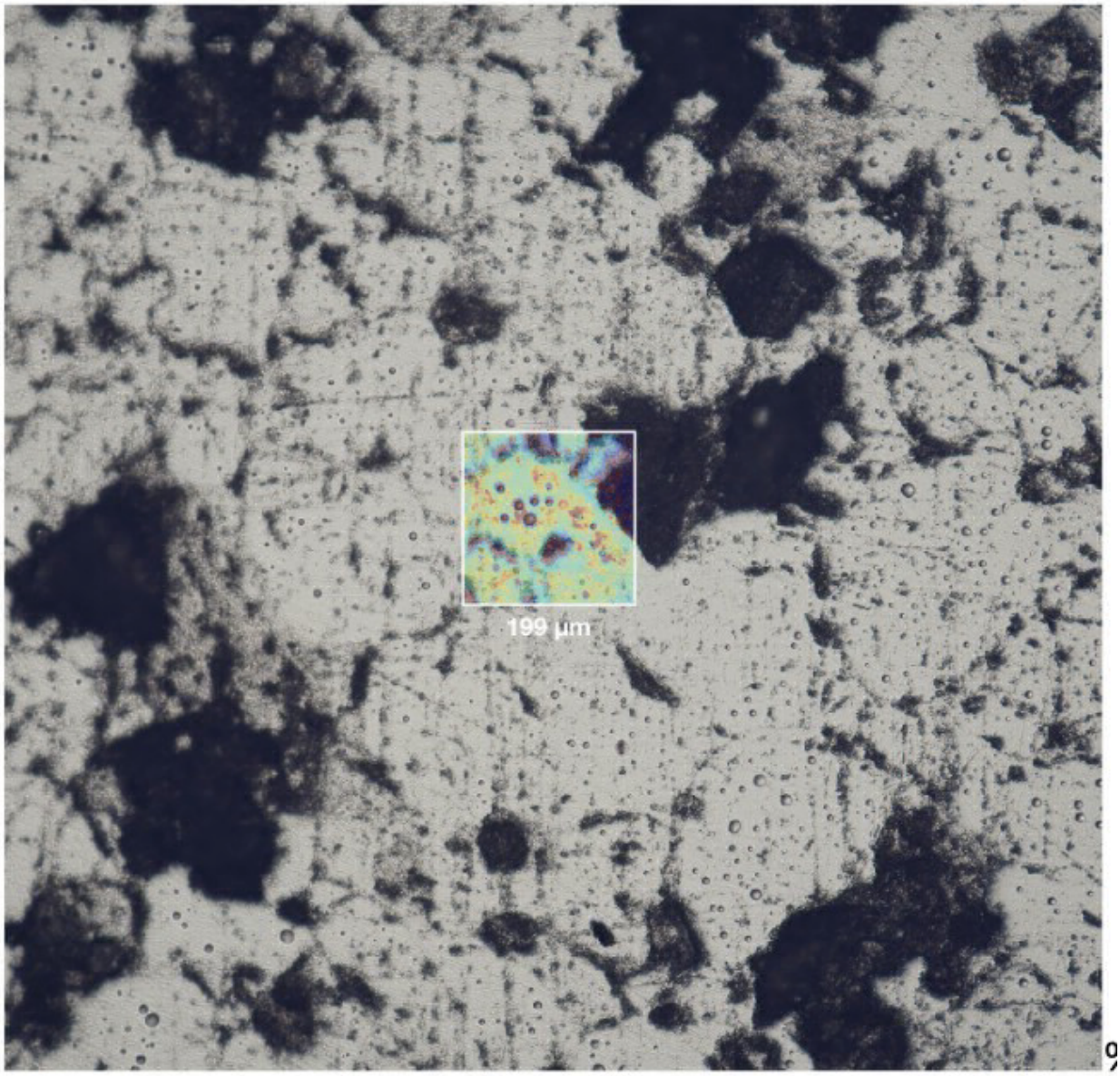

Figure A.13: Picture of the whole polished face of the specimen. The boxed section indicates the location the testing was done.

---

k_cross : 8.46 W/m·K ± 21%
k_in : 5.15 W/m·K ± 29%

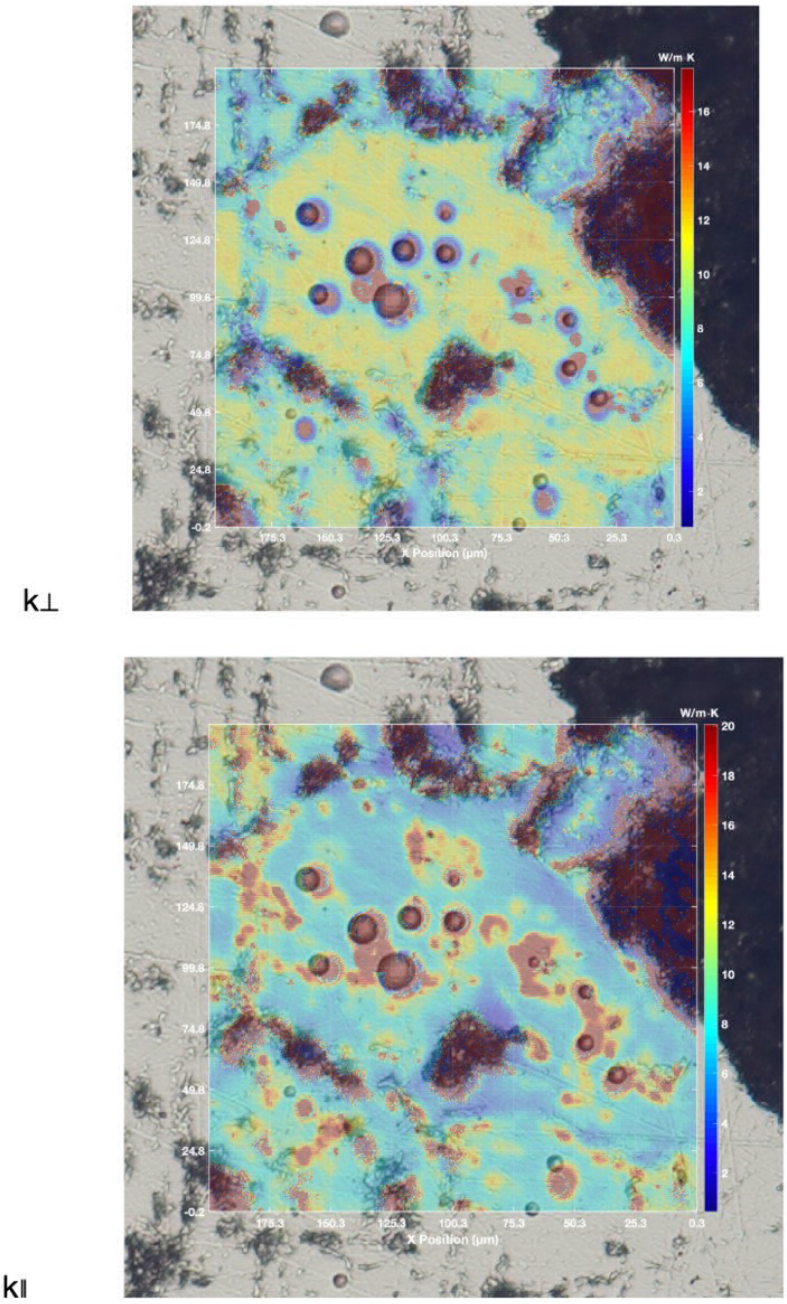

Figure A.14: Close-up thermal map of the section of rock tested with both in-plane and cross-plane thermal conductivities. In plane indicated the thermal conductivity that is parallel to the rock surface and cross-plane is perpendicular to the rock surface. A blue color indicates a lower thermal conductivity and red indicates a higher thermal conductivity.

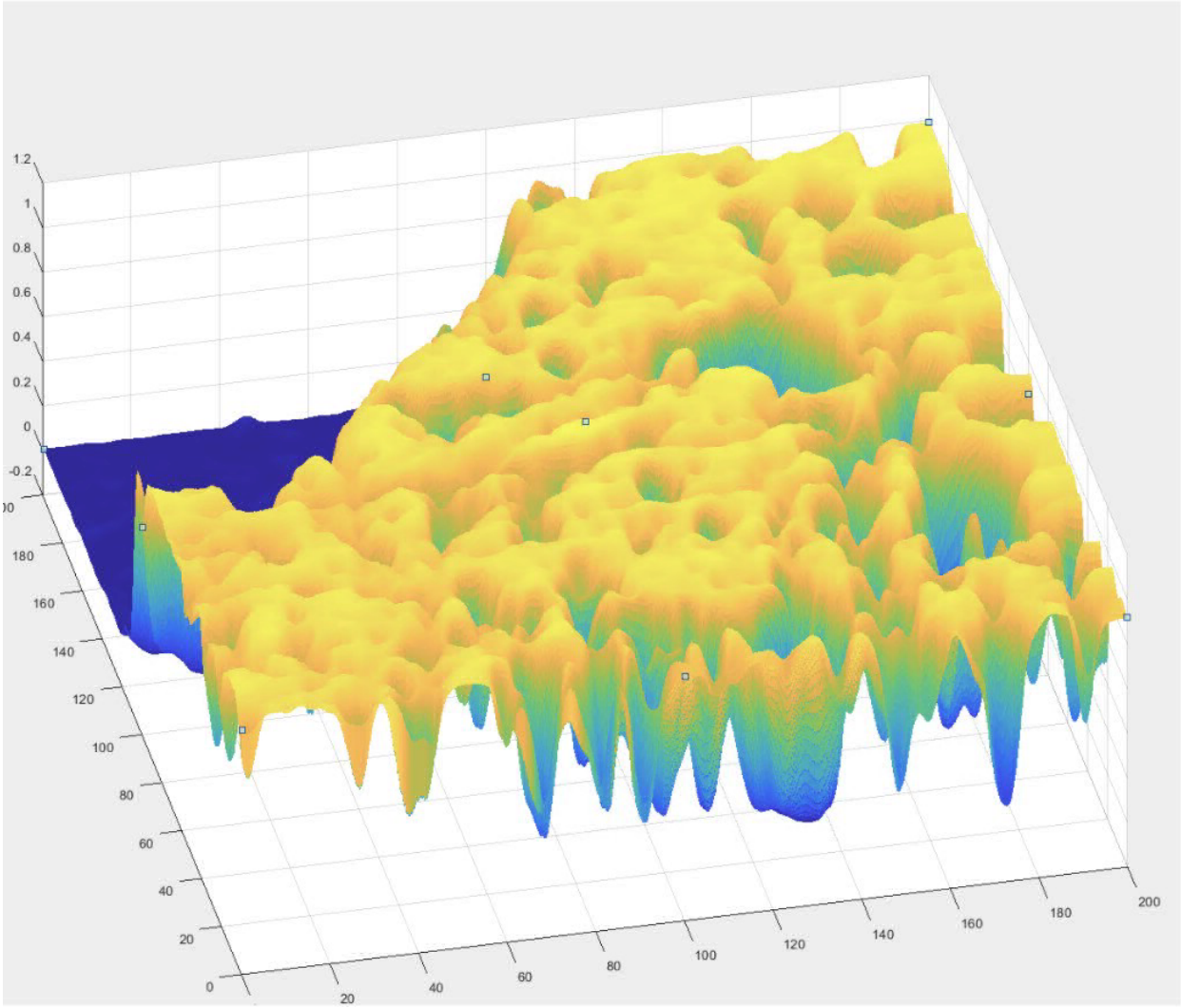

Figure A.15: Contour plot showing the surface topography taken from the section of the specimen that was measured (boxed section in Figure A.13). Blue indicates deeper void spaces.

A.5 Conclusions

In this research, triaxial, heat capacity, and thermal conductivity tests were conducted. The following interpretation can be made.

- In the creep stage, during the triaxial testing, the axial creep rate decreased with time.
- The Young's modulus of this sandstone specimen (47 GPa) is on the higher side of

the average Youngs Modulus values for sandstone.

- The heat capacity is also higher in this sandstone specimen than that of the basalt and granite analyzed in a previous MM-Wave study.
- The thermal conductivity of the sandstone is in the average range for quartz based sandstones.

Bibliography

[1]E. Barbier, "Geothermal energy technology and current status: an overview", Renewable and Sustainable Energy Reviews **6**, 3–65 (2002).

[2]A. M. Omer, "Geothermal Energy Used in Buildings Heating and Cooling", en,

[3]P. Ledru and L. Guillou Frottier, "Reservoir Definition", en, in *Geothermal Energy Systems*, Section: 1 _eprint: https://onlinelibrary.wiley.com/doi/pdf/10.1002/9783527630479.ch1 (John Wiley & Sons, Ltd, 2010), pp. 1–36.

[4]S.-Y. Pan, M. Gao, K. J. Shah, J. Zheng, S.-L. Pei, and P.-C. Chiang, "Establishment of enhanced geothermal energy utilization plans: Barriers and strategies", en, Renewable Energy **132**, 19–32 (2019).

[5]T. Gupta, C. Maji, R. Gupta, R. Das, and H. Chaudhuri, "Green Energy and Sustainable Environment", in (May 2016).

[6]*Geothermal Energy: A Glance Back and a Leap Forward*, en.

[7]S. Naganawa, "Survey on Effective and Feasible Emerging Technologies for EGS Well Drilling", in (2015).

[8]E. Fjær, R. M. Holt, P. Horsrud, and A. M. Raaen, *Petroleum Related Rock Mechanics*, en, Google-Books-ID: l6CfasFxhzYC (Elsevier, Jan. 2008).

[9]*Fig. 1. schematic of wellbore stability and instability intervals*, en.

[10]F. Bin and W. Pao, *Mud Weight Prediction for Offshore Drilling* (May 2012).

[11]D. Patel, V. Thakar, S. Pandian, M. Shah, and A. Sircar, "A review on casing while drilling technology for oil and gas production with well control model and economical analysis", en, Petroleum **5**, 1–12 (2019).

[12]P. P. Woskov, "Gyrotron Based Melting", eng, in *78th Conference on Glass Problems* (John Wiley & Sons, Inc, Hoboken, NJ, USA, 2018), pp. 233–246.

[13]S. Selvini, *GAPSTI and Quaise Energy Inc. co-fund clean energy project at the Laboratory for Scientific Computing*, en-GB, Mar. 2021.

[14]X. Chen, Y. Zhang, D. Hui, M. Chen, and Z. Wu, "Study of melting properties of basalt based on their mineral components", Composites Part B: Engineering **116**, 53–60 (2017).

[15]N. L. Bowen, "The Behavior of Inclusions in Igneous Magmas", The Journal of Geology **30**, Publisher: The University of Chicago Press, 513–570 (1922).

[16]S. J. B. Reed, *Electron Microprobe Analysis and Scanning Electron Microscopy in Geology*, en (Cambridge University Press, Aug. 2005).

[17]K. Janssens, "Chapter 4 X-ray based methods of analysis", in *Comprehensive Analytical Chemistry*, Vol. 42, Non-Destructive Microanalysis of Cultural Heritage Materials (Elsevier, Jan. 2004), pp. 129–226.

[18]S. D. Viktorov, Y. I. Golovin, A. N. Kochanov, A. I. Tyurin, A. V. Shuklinov, I. A. Shuvarin, and T. S. Pirozhkova, "Micro- and nano-indentation approach to strength and deformation characteristics of minerals", en, Journal of Mining Science **50**, 652–659 (2014).

[19]W. C. Oliver and G. M. Pharr, "Measurement of hardness and elastic modulus by instrumented indentation: Advances in understanding and refinements to methodology", en, Journal of Materials Research **19**, 3–20 (2004).

[20]W. Kiefer, "The Raman effect-a unified treatment of the theory of Raman scattering by molecules. Derek A. Long, John Wiley & Sons, Ltd., 2002, Pp 597. ISBN 0-471-49028-8",

eng, Journal of Raman Spectroscopy **34**, Place: Chichester, UK Publisher: John Wiley & Sons, Ltd, 180–180 (2003).

[21] J. Toporski, T. Dieing, and O. Hollricher, eds., *Confocal Raman Microscopy*, en, Vol. 66, Springer Series in Surface Sciences (Springer International Publishing, Cham, 2018).

[22] *Elemental mapping (EDS) — Glossary — JEOL Ltd.* en.

[23] S. V. Hainsworth, H. W. Chandler, and T. F. Page, "Analysis of nanoindentation load-displacement loading curves", en, Journal of Materials Research **11**, 1987–1995 (1996).

[24] J. M. Maragh, "A multiscale framework for the chemomechanical characterization of ancient heterogeneous materials", eng, Accepted: 2021-05-25T18:21:25Z, Thesis (Massachusetts Institute of Technology, 2021).

[25] E. Johnson, "7.3 The Raman Shift and Reading Raman Spectra", en, Book Title: Analytical Methods in Geosciences.

[26] B. Karmakar, "Chapter 1 - Fundamentals of Glass and Glass Nanocomposites", in *Glass Nanocomposites*, edited by B. Karmakar, K. Rademann, and A. L. Stepanov (William Andrew Publishing, Boston, Jan. 2016), pp. 3–53.

[27] S. Ahmed and S. Salehi, "Failure Mechanisms of the Wellbore Mechanical Barrier Systems: Implications for Well Integrity", Journal of Energy Resources Technology **143**, 10.1115/1.4050694 (2021).

[28] H. Kang, "Numerical and Experimental Study of Rock Fracture Creep Under Dry Conditions", en, Accepted: 2022-01-14T14:55:43Z, Thesis (Massachusetts Institute of Technology, June 2021).